Mesoscale Eddies and *Trichodesmium* spp. Distributions in the Southwestern North Atlantic

Elise M. Olson,[1] Dennis J. McGillicuddy,[1] Glenn R. Flierl,[2] Cabell S. Davis,[1]

Sonya T. Dyhrman,[3] and John B. Waterbury[1]

Corresponding author: Elise M. Olson, MS#11, Woods Hole Oceanographic Institution, Woods Hole, MA 02543, USA. (eolson@whoi.edu)

[1]Woods Hole Oceanographic Institution, Woods Hole, USA.

[2]Department of Earth, Atmospheric and Planetary Sciences, Massachusetts Institute of Technology, Cambridge, Massachusetts, USA.

[3]Dept. Earth and Environmental Science and the Lamont-Doherty Earth Observatory, Palisades, New York, USA.

Abstract. Correlations of *Trichodesmium* colony abundance with the eddy field emerged in two segments of Video Plankton Recorder observations made in the southwestern North Atlantic during fall 2010 and spring 2011. In fall 2010, local maxima in abundance were observed in cyclones. We hypothesized surface Ekman transport convergence as a mechanism for trapping buoyant colonies in cyclones. Idealized models supported the potential of this process to influence the distribution of buoyant colonies over timescales of several months. In spring 2011, the highest vertically integrated colony abundances were observed in anticyclones. These peaks in abundance correlated with anomalously fresh water, suggesting riverine input as a driver of the relationship. These contrasting results in cyclones and anticyclones highlight distinct mechanisms by which mesoscale eddies can influence the abundance and distribution of *Trichodesmium* populations of the southwestern North Atlantic.

1. Introduction

Trichodesmium is a genus of nitrogen-fixing cyanobacteria found throughout the tropical and subtropical oceans. Converting atmospheric dinitrogen into biologically available forms, it represents an important source of new nitrogen to oligotrophic regions and contributes to primary production [*Capone et al.*, 1997; *Carpenter*, 1983; *LaRoche and Breitbarth*, 2005; *Letelier and Karl*, 1996]. Therefore, *Trichodesmium* potentially contributes to carbon export from the surface waters [*Capone et al.*, 1998; *Dore et al.*, 2002; *Bar-Zeev et al.*, 2013]. Thus, understanding the controls on *Trichodesmium* abundance and distribution is a step toward quantifying the contribution of *Trichodesmium* to oceanic nitrogen and carbon cycling.

On a Video Plankton Recorder (VPR) survey across the North Atlantic subtropical gyre, *Davis and McGillicuddy* [2006] identified a correlation between *Trichodesmium* colony abundance and sea level anomaly. Greater abundances were observed in warm and salty anticyclonic eddies. Other observations of elevated *Trichodesmium* abundance in anticyclones have been made in the Pacific [*Fong et al.*, 2008] and eastern North Atlantic [*Taboada et al.*, 2010]. To investigate the spatial and temporal generality of this pattern, we analyzed relationships between *Trichodesmium* colony distributions and the mesoscale eddy field based on sea level anomaly and VPR data from two cruises, in fall 2010 and spring 2011. The cruises took place in the southwestern North Atlantic, typically a region of high *Trichodesmium* abundance.

There was no single, ubiquitous relationship between mesoscale dynamics and colony abundance. However, patterns emerged within localized regions on the two cruises, with

elevated abundances in cyclonic eddies during the fall, and in fresh, anticyclonic eddies during the spring. These two patterns are both distinct from the association with warm, salty anticyclones *Davis and McGillicuddy* [2006] observed farther north and east in the subtropical North Atlantic. Here we attempt to explain these relationships through analysis of the physical processes underlying each.

In the following section we present a brief overview of observational methods employed during the fall and spring cruises. Then we summarize the fall 2010 observations of elevated *Trichodesmium* colony abundances in cyclonic eddies and present a hypothesis of wind-driven concentration as a driving mechanism. We evaluate this idea through an idealized conceptual model and through a series of more realistic numerical simulations, leading to an analysis of the potential of this mechanism to produce the observed patterns. Then, we turn to the contrasting spring 2011 observations of elevated *Trichodesmium* colony abundances in anticyclonic eddies. We associate this pattern with a correlation between *Trichodesmium* abundance and fresh water influence [e.g. *Subramaniam et al.*, 2008] and investigate the relationship between phosphorus salinity in the region. Finally, we conclude by suggesting circumstances under which these two differing patterns of correlation with the mesoscale eddy field might emerge.

2. Observational Methods

Sampling occurred on two cruises on the R/V *Oceanus*, OC469 from October 1–22, 2010, and OC471 from April 23–May 13, 2011, beginning near Bermuda and ending near Barbados (Figure 1). Precise sampling locations were chosen during the cruises as informed by satellite observations of sea surface height, real-time analysis of VPR *Trichodesmium* abundance observations, and ocean-color–based estimates of *Trichodesmium* bloom prob-

ability [*Westberry and Siegel*, 2006; *Westberry et al.*, 2005]. This adaptive strategy allowed sampling to be directed toward interesting physical and biological features such as eddies and areas of predicted *Trichodesmium* abundance. *Trichodesmium* colony abundance was sampled by the VPR, towed between stations (Figure 1). As a result of the timing of station work, a majority of VPR sampling occurred in late afternoon and throughout the night.

The VPR consists of a towed body, containing a CTD and a synchronized video camera and xenon strobe [*Davis et al.*, 2005]. Data are sent in real-time through a fiber-optic cable to a shipboard computer system. The VPR undulated between the surface (5–10 m) and approximately 120 m depth, completing an up-down cycle approximately every six minutes, corresponding to one vertical cycle every 1.8 km at 10 knots (5.1 $\mathrm{m\,s^{-1}}$). At a frame rate of 30 Hz, each 984 x 1009 pixel video frame was passed through object-identification software to pick out "regions of interest", which were saved, using a time-stamp naming convention, to a hard disk.

Images were initially sorted using image recognition software [*Hu and Davis*, 2006]. For the spring cruise, due to the large number of images collected, the sample size was reduced to 1000 images per sampling hour, evenly spaced among the collected images [*Olson*, 2014]. For both cruises, each machine-classified image was manually checked and reclassified as necessary, into the three *Trichodesmium* morphological categories, puff, raft, and bowtie, and an "other" category containing everything else. *Trichodesmium* puff, raft, and bowtie colonies are readily sampled using the VPR system due to their macroscopic size, but free-living individual trichomes are not distinguishable from other objects of similar shape and size.

The volume of the field of view of was calibrated before each cruise by the tethered copepod method described by *Davis et al.* [2005] and was 6.929 mL and 15.168 mL during the fall and spring cruises, respectively. These volumes were used to convert observation frequencies to abundances. The corresponding vertical and horizontal dimensions of the field of view were 13 mm x 13 mm and 12 mm x 12 mm; the camera and strobe were oriented to produce a deeper and narrower field of view for the spring cruise. Abundance data were gridded to bins 5 m deep and 11 and 33 km wide for the fall and spring cruises, respectively. Within each bin, abundances were estimated under the assumption of a Poisson distribution, based on the summed image volume and the number of positive identifications.

In addition to imaging, the VPR contained a CTD probe that recorded pressure, temperature, salinity, photosynthetically active radiation (PAR), oxygen (on the spring cruise only), and fluorescence. Physical and bio-optical data from the VPR were binned to the same horizontal resolution as the abundance data and either 1 or 5 m vertically, as indicated.

At each hydrographic station in between VPR tows, CTD casts measured temperature, salinity and PAR. 125 ml water samples collected at depths of 700, 500, 300, 200, 100, 80, 60, 40, 20 m, and the surface were filtered through 0.2 μm , 47 mm polycarbonate filters and stored frozen at -20 °C in 10% HCl-cleaned bottles prior to nutrient analysis. Phosphate [PO4] and total dissolved phosphorus [TDP] were analyzed at the Chesapeake Bay Lab at the University of Maryland using standard autoanalyzer protocols (nasa.cbl.umces.edu). For samples in the upper 100 m, low level phosphate concentration was measured using a modified MAGIC method (Rimmelin and Moutin, 2005). Dissolved

organic phosphorus (DOP) was assessed as the difference between total and inorganic pools. Alkaline phosphatase activity (APA) was measured using a fluorescent substrate analog after *Dyhrman and Ruttenberg* [2006]. Measurement detection and quantification limits were: PO_4 DL=0.0025 μM, QL=0.08 μM; TDP DL=0.05 μM, QL=1.45 μM.

In the upper 80 m, water samples were gravity filtered and preserved for microscopic enumeration of both *Trichodesmium* colonies and free trichomes. Microscopic colony counts were compared to VPR colony abundances and agreed well for VPR-based abundances below 1.5 colonies L^{-1} [*Olson*, 2014]. Above 1.5 colonies L^{-1}, VPR-based abundances were biased low but still showed, overall, a positive relationship with abundances from microscopic enumeration. VPR-based abundances above approximately 1.5 colonies L^{-1} should be interpreted cautiously, although patterns may be inferred.

Throughout the cruise, underway sensors measured near-surface environmental conditions. Currents were measured by ADCP. Wind speeds were measured by sensors mounted at 15 m above sea level on the port and starboard sides of the ship. Temperature profiles were recorded using XBTs deployed approximately every hour while underway.

Sea level anomaly (SLA) and absolute dynamic topography (ADT) along the cruise tracks were estimated by linear interpolation in space and time from objectively analyzed fields. The objective analysis combines altimetric data from Envisat, Jason-1 and Jason-2. Eddies were tracked in time and space by visually comparing daily objectively analyzed SLA fields.

3. Enhanced Abundance of *Trichodesmium* Colonies in Cyclones

A roughly 700 km region (Section 2 in Figure 1) where *Trichodesmium* colony abundance patterns reflected variations in sea level anomaly associated with the eddy field was

transected during the fall cruise (OC469). There, in contrast to observations made in Spring 2011 and previously in the subtropical North Atlantic [*Davis and McGillicuddy*, 2006], *Trichodesmium* colony abundances were locally elevated in cyclones and nearly absent outside of them. Over this region (Section 2, Figures 1 and 2), the correlation coefficient between interpolated sea level anomaly and integrated *Trichodesmium* abundance was -0.67 ($p<0.01$). Surface abundances within the two cyclones (C3 and C in Figure 2) fell in the range of 0.2–0.7 colonies L^{-1}, compared to a range from below the limit of detection to 0.2 colonies L^{-1} in the anticyclones (AC3 and AC4).

Abundances throughout this region were low compared to elsewhere on the cruise, with surface colony abundances averaging 0.8 colonies L^{-1} to the north and 2.0 colonies L^{-1} to the south. Rafts were the dominant morphology and were vertically distributed differently from the other morphologies, with greatest abundance within the surface mixed layer. On the southwest side of the center of Eddy C3, depth-integrated colony abundances in the closest four 11-km grid cells to the center averaged 12.7×10^3 colonies m^{-2}. Integrated colony abundances in the seven 11-km grid cells closest to the center of eddy A3 averaged 0.85×10^3 colonies m^{-2}.

At the time of sampling, Eddy C3 had a diameter of roughly 150 km based on the largest closed encircling SLA contour. Although the eddy was not symmetric in shape, a representative radius at which maximum velocities were found was approximately 50 km. Based on shipboard ADCP measurements, maximum velocities at approximately 20-30 m depth were 0.13 m s^{-1} on the western side and of the eddy and 0.45 m s^{-1} on the eastern side.

3.1. Hypothesis: Concentration of Buoyant Particles Through Convergent Ekman Transport in Cyclones

Association of *Trichodesmium* abundance with cyclones was unexpected, as previously greater abundances were observed in anticyclones [*Davis and McGillicuddy*, 2006; *Fong et al.*, 2008; *Taboada et al.*, 2010]. In some cases, nutrient injection as isopycnals dome upward during eddy formation, with associated shoaling of the nutricline, has been invoked to explain elevated phytoplankton abundance in cyclones [e.g. *Falkowski et al.*, 1991; *McGillicuddy and Robinson*, 1997]. Here, however, the inorganic phosphorus pool is deep compared to the location of *Trichodesmium* colonies, found mostly within the mixed layer, and iron is thought to be supplied primarily from surface deposition. In fact, rafts, the most buoyant of *Trichodesmium* colony morphologies, dominated in this region. The buoyancy of *Trichodesmium* colonies and their surface-intensified depth distribution led to a hypothesis of physical concentration by convergent wind-driven surface currents in cyclones.

The hypothesis of wind-driven accumulation of buoyant *Trichodesmium* colonies in cyclones is based on convergent transport in cyclonic eddies due to variations in wind stress across the breadth of an eddy. These wind stress variations result from the difference in the surface currents on opposite sides of the eddy (Figure 3). Since wind stress depends on the relative velocity between air and ocean, it will be greater where the current flows opposite to the wind. As a result, in the surface boundary layer of a cyclone, more water flows into the cyclone on the side where current and wind are in opposition than flows out on the side where current and wind are parallel. This results in surface convergence, balanced by downward motions in the eddy interior. The opposite takes place in anti-

cyclones, with wind-driven surface divergence leading to upwelling. We will refer to this effect as "eddy–wind interaction" throughout. Vertical velocities due to this type of spatial variation in Ekman transport have been identified previously [*McGillicuddy et al.*, 2007; *Ledwell et al.*, 2008] as a mechanism for nutrient supply in anticyclonic and mode-water eddies, and the physical mechanism has been well described [*Dewar and Flierl*, 1987; *Martin and Richards*, 2001].

3.2. Theoretical Model

Martin and Richards [2001] investigated eddy–wind interaction in the context of an eddy with Gaussian velocity structure at the surface. This idealized eddy surface velocity field reflects solid body rotation at the eddy center and exponential decay beyond the radius of maximum velocity. The azimuthal velocity is

$$\mathbf{v}_\theta(r) = V\frac{r}{R}\exp\left[\frac{1}{2}\left(1-\frac{r^2}{R^2}\right)\right], \tag{1}$$

where V is the maximum azimuthal velocity, which occurs at a radius $r = R$ from the eddy center. In the northern hemisphere, V is positive in a cyclonic eddy.

The formula for the steady Ekman transport is

$$\mathbf{U_E} = (U_E, V_E) = \left(\frac{\tau^{(y)}}{\rho_0 f}, -\frac{\tau^{(x)}}{\rho_0 f}\right) \tag{2}$$

(see *Batchelor* [1967] equation 4.4.II), where ρ_0 is the density of seawater (1026 $\mathrm{kg\,m^{-3}}$), and f is the Coriolis parameter (5.21×10^{-5} $\mathrm{s^{-1}}$). $\tau^{(x)}$ and $\tau^{(y)}$ are the zonal and meridional components of the wind stress at the ocean surface.

Dewar and Flierl [1987] used the wind stress paramaterization,

$$\tau = \rho_a c_d |\mathbf{U_a} - \mathbf{u}|(\mathbf{U_a} - \mathbf{u}), \tag{3}$$

where ρ_a is the density of air (1.2 kg m^{-3}); c_d is the drag coefficient (0.00118); $\mathbf{U_a}$ is the wind velocity; and $\mathbf{u}$ is the sea surface velocity. They assumed a uniform westerly wind and small eddy surface velocities compared to wind velocity ($|u| \ll |U_a|$), so that the wind stress expression was simplified to

$$\left(\tau^{(x)}, \tau^{(y)}\right) = \left(\rho_a c_d (U_a^2 - 2U_a u_0), -\rho_a c_d U_a v_0\right), \tag{4}$$

where u_0 and v_0 are the zonal and meridional components of the azimuthal sea surface velocity associated with the eddy ($\mathbf{v}_\theta$, Equation 1). Then, the zonal and meridional components of the Ekman transport are

$$U_E = -\frac{\rho_a c_d}{\rho_0 f} U_a v_0, \tag{5}$$

and

$$V_E = -\frac{\rho_a c_d}{\rho_0 f} (U_a^2 - 2U_a u_0). \tag{6}$$

The first term contributing to V_E (Equation 6) is the nondivergent wind stress in the absence of sea surface motion. The second term in V_E and the single term contributing to U_E (Equation 5) reflect modification of the wind stress by the sea surface velocity. In a cyclonic eddy, these terms produce convergence at the eddy center, leading to downwelling there (see *Dewar and Flierl* [1987]).

Buoyant particles tend to concentrate in regions of surface convergence; they are advected laterally, but float rather than following water trajectories leaving the surface (Figure 3). Similarly, buoyant particles become spread out in regions of surface divergence. This phenomenon has previously been investigated in the context of frontal dynamics [*Franks*, 1992]. Additionally, submesoscale modeling of effects of surface convergence and divergence on buoyant particle fields has demonstrated expulsion from anticyclones and

concentration in regions of convergence [*Zhong et al.*, 2012]. Here, we expect the convergence of Ekman transport to lead to concentration of *Trichodesmium* colonies in cyclones (Figure 3), as previous investigation of *Trichodesmium* colony floating velocities indicated that a majority of colonies were positively buoyant [*Walsby*, 1978]. Thus, the effect could lead to higher concentrations of buoyant *Trichodesmium* colonies in cyclones than anticyclones, consistent with the observed distribution of *Trichodesmium* colonies in relation to the mesoscale eddy field in fall 2010.

We here present an idealized analytical model for the change in concentration of buoyant tracer over time, based on the convergence of Ekman transport near the center of a cyclonic eddy (Section 3.1). For the purpose of these calculations, we supposed that the horizontal Ekman transport occurrs over an initially vertically homogeneous surface layer of depth H containing uniform tracer concentration. We further supposed that over time, the tracer maintains its position vertically, and is thus subject to horizontal but not vertical advection. Thus, in the absence of diffusive mixing, the fractional change in concentration along a Lagrangian path is proportional to the opposite of the divergence of the velocity field.

$$\frac{1}{C}\frac{DC}{Dt} = -\nabla \cdot \mathbf{u}_h, \tag{7}$$

where $\nabla \cdot \mathbf{u}_h$ is the divergence of the horizontal velocity field, C is concentration, and $\frac{D}{Dt}$ denotes the Lagrangian derivative. In regions of convergence, tracer maintains its position as the fluid stretches vertically, so tracer concentration increases. In regions of divergence, tracer-free water is injected into the upper layer, decreasing local tracer concentration. The velocity in this layer, $\mathbf{u}$, with components u and v, is the sum of the azimuthal eddy surface velocity (Equation 1) and the Ekman transport (Equations 5 and 6) divided by

the layer depth, H:

$$u = u_0 + u_E = -v_\theta \sin\theta - \frac{\rho_a c_d}{\rho_0 f H} U_a v_0 \tag{8}$$

$$v = v_0 + v_E = v_\theta \cos\theta - \frac{\rho_a c_d}{\rho_0 f H}(U_a^2 - 2U_a u_0) \tag{9}$$

Integration of this velocity field reveals that in a cyclone, trajectories originating close to the eddy center are trapped within the eddy, slowly spiraling inward toward the center (Figure 4).

We were interested in the overall change in tracer concentration over the eddy core, which we defined as the region within the radius of maximum velocity ($r < R$). The horizontal velocity divergence is equal to the Ekman pumping, w_e,

$$w_e = \frac{\rho_a}{\rho_0 f_0} c_d U_a (2(u_E)_y - (v_E)_x) \tag{10}$$

[*Dewar and Flierl*, 1987].

We estimated the horizontal flux of water into an eddy, F, as the opposite of the Ekman pumping integrated over the eddy core.

$$F = \frac{\rho_a}{\rho_0 f_0} c_d U_a 3\pi R V. \tag{11}$$

At time $t = 0$, if *Trichodesmium* colonies were spread uniformly throughout the surface layer with a concentration C_0, the initial flux of colonies into the eddy center would be $\phi = C_0 F$. Then, the fractional rate of change of integrated abundance within the eddy would be

$$\frac{1}{C_0}\frac{\mathrm{d}C}{\mathrm{d}t} = \frac{3\rho_a c_d U_a V}{\rho_0 f_0 R H}. \tag{12}$$

Using parameters from Table 1, based on Eddy C3, the initial relative rate of increase of concentration within the center of the cyclone would be 0.5% per day.

Over time, additional factors influence the flux of tracer into the eddy. The tracer concentration itself develops spatial variability, which precludes application of Equation 12. As gradients in tracer concentration develop, diffusive processes will tend to counteract them. Additionally, on the northern and southern flanks of the eddy (Figure 4a), the horizontal velocity field described by Equations 8 and 9 has regions of divergence. Tracer concentrations decrease along trajectories as they pass through those regions, eventually influencing conditions in the eddy as those trajectories continue into the center region.

Many factors not represented in this simplified analytical model could be simulated more realistically in a numerical model. These include time dependent eddy dynamics (e.g. eddy decay) as well as the effects of continuous and evolving spatial variability in tracer distribution. Additionally, small differences were anticipated due to the neglected higher order terms in the wind stress formulation (Equations 3 and 4).

3.3. Numerical Model

The rate of wind-driven accumulation of buoyant particles, such as *Trichodesmium* colonies, in the center of a cyclonic eddy was investigated with a series of numerical simulations using a three-dimensional primitive equation model. The core numerical experiment consisted of a pair of simulations of cyclonic eddies with different surface wind stress formulations. In one simulation, surface stress was calculated based solely on surface wind velocities. In the other, more realistic, parameterization, surface stress was related to the relative air-sea velocity at the surface (Equation 3). Thus, in the first simulation, the mechanism illustrated in Figure 3 and referred to throughout as "eddy–wind interaction" was turned off, and in the second it was turned on. Buoyant colonies were represented by a tracer with an imposed upward velocity. By comparing the two simulations, we assessed

the extent to which spatial variation in wind stress due to eddy surface velocities could drive concentration of buoyant colonies in cyclonic eddies. Additional simulations were carried out to investigate the sensitivity of the results to the floating velocity and strength of the simulated eddy as well as the behavior of the eddy in the absence of wind (Table 2).

3.3.1. Model Configuration

Each simulation contained an isolated eddy within a doubly periodic domain. The model implementation was nearly identical to that described by *Ledwell et al.* [2008]. The model was the Los Alamos Parallel Ocean Program (POP) version 2, a three-dimensional primitive equation model employing the hydrostatic and Boussinesq approximations [*Smith et al.*, 2000]. Horizontal mixing of momentum and tracers was Laplacian with diffusivity and kinematic viscosity of 1 $m^2 s^{-1}$. The model included k-profile vertical mixing with a background diffusivity of 10^{-5} $m^2 s^{-1}$. Tracer advection was by a centered difference scheme (MPDCD) with a flux limiter to prevent negative concentrations. Simulations were carried out on an f-plane, at 21°N, to avoid westward translational motion of the eddies due to the variation in planetary vorticity with latitude and facilitate model diagnosis in eddy-centric coordinates. The vertical grid contained 72 levels with resolution increasing from 125 m at 4462 m depth to 5 m at the surface. Horizontally, the doubly periodic domain contained 141×141 cells with zonal and meridional resolution of approximately 3.1 km.

We used the POP version 2 free surface boundary condition. Restoring freshwater and heat fluxes at the surface were applied on timescales of 1 day. Wind stress was formulated as in *Ledwell et al.* [2008], with parameterizations for uniform and surface-

current–dependent stress. Wind speed was constant at 4.7 $\mathrm{m\,s^{-1}}$, rotating in direction on a 64 hour cycle to avoid net Ekman transport in the horizontal direction. The chosen wind speed was the average wind speed observed during the fall cruise for the period October 9–15, 2010, when the ship was near the region where elevated *Trichodesmium* colony abundance was observed in cyclones.

As in *Ledwell et al.* [2008], hydrographic profiles from the center and periphery of an observed eddy were used to initialize the model temperature and salinity fields (Auxiliary Material, Figure A.1), with Gaussian interpolation between center and edge profiles with an e-folding scale of 68 km. The eddy simulated was Cyclone C3 from the fall cruise (Figure 1). A station was located at the center of Eddy C3, so CTD measurements were available there to 700 m. CTD temperature and salinity measurements from the VPR were available in the upper 150 m at the edge location. At the edge, XBT temperature measurements were available to 700 m. Salinity between 150 m and 700 m was inferred based on the temperature-salinity relationship observed at Station 8, at the eddy center. Below 700m at both center and edge, climatological values based on the World Ocean Atlas 2009 [*Antonov et al.*, 2010; *Locarnini et al.*, 2010] were used.

Initial velocity fields were calculated based on geostrophic and cyclostrophic balance with zero motion at the lowermost model level. Whereas addition of a barotropic velocity component brought velocity fields into agreement with observations in the *Ledwell et al.* [2008] eddy simulation, such an addition was not required here. The velocity structure was characterized by solid body rotation in the eddy core transitioning to exponential decay with increasing distance from the eddy center. A maximum azimuthal velocity of

0.22 m s^{-1} occurred at a radius of 48 km, roughly consistent with ADCP measurements of velocities associated with Eddy C3.

Trichodesmium colony buoyancy was simulated by imposing an upward vertical tracer velocity at every location except the surface boundary. Buoyant *Trichodesmium* colonies have been observed to rise at velocities greater than 0.001 m s^{-1} (90 m d^{-1}) [*Walsby*, 1992]. However, a large range of velocities may be measured in a given location, some positive and some negative. In one study [*Walsby*, 1978], 69% of *T. thiebautii* (puff) colonies, 87% of *T. contortum* (raft) colonies, and 100% of *T. erythraeum* (raft) colonies were positively or neutrally buoyant. In a sample collected at 20 m, *Walsby* [1978] measured floating velocities of *T. thiebautii* (puff) colonies with a range of $\pm 7\times10^{-4}$ m s^{-1} and a mean velocity of -3×10^{-5} m s^{-1} . Mean observed raft velocities were not specified, but it seems reasonable to assume they were positive, based on the greater proportion of floating raft colonies compared to puff colonies. Based on these data, a model tracer velocity of 1.2×10^{-4} m s^{-1} (10 m d^{-1}) was chosen for the present study, with sensitivity analyses conducted at 1.2×10^{-3} and 1.2×10^{-5} m s^{-1}.

As the velocity fields used to initialize the model were in approximate balance, an initial adjustment of velocity and density structure took place at the beginning of the model run, with the largest changes taking place on the first day. To avoid influence of this initial adjustment period on the results, the tracer concentration was reset after 8 days of simulation and the model restarted. Therefore, in the results that follow, time is referenced to the restart day rather than the day on which the model physics were initialized. As a result, maximum azimuthal eddy velocities on day 1 differ from those

calculated in the initial conditions, changing from 0.22 to 0.23 $\mathrm{m\,s^{-1}}$ in the cyclone with eddy–wind interaction and to 0.24 $\mathrm{m\,s^{-1}}$ in the cyclone without eddy–wind interaction.

The tracer initial condition consisted of constant concentration throughout the upper 20 m of the model domain. This placed the tracer initially within the mixed layer, reducing the time for the tracer to adjust to its quasi-equilibrium vertical distribution, a balance between floating velocity, vertical fluid velocity, and vertical mixing. This vertical distribution was achieved within the first day of simulation, so that by day two the daily average vertical distribution of colonies was within 1.4% of its quasi-equilibrium distribution, based on the distribution at the end of the initial adjustment period.

3.3.2. Numerical Model Results

Time-mean cross sections revealed the impact of eddy–wind interaction on simulated tracer distributions (Figure 5). In the simulation without eddy–wind interaction, mixed layer depth was shallower inside the core of the cyclone than outside it. Therefore, buoyant tracer mixed vertically over a shorter distance inside the cyclone, producing a local maximum in surface tracer concentration at the eddy center. This is why concentration increased at the surface in the center of the eddy, even though integrated tracer concentrations were roughly constant throughout the model domain. Net flux into the eddy across a circle of radius of 48 km (approximately the radius associated with maximum eddy velocity) was nearly zero throughout the upper 50 meters (Figure 6).

Compared to the cyclone without eddy–wind interaction, the cyclone with eddy–wind interaction exhibited less doming of the pycnocline as demonstrated by the mixed layer depth (Figure 5). This flattening of isopycnals resulted from downward motion within the eddy due to convergent Ekman transport. The inward volume flux associated with these

downward motions was concentrated in the upper 25 m (Figure 6) and led to accumulation of buoyant tracer near the cyclone center. This horizontal convergence of buoyant tracer was associated with a maximum in integrated tracer concentration at the center of the eddy (Figure 5, lower left). In both cases, with and without eddy–wind interaction, the mean mixed layer depth deepened over the course of the simulations, from initial conditions with weak surface stratification to a mixed layer of approximately 30 m by day 50.

We assessed the accumulation of tracer as the percent difference in mean integrated concentration within the core ($r < 48$ km) from that of the initial condition (Figure 7). In the cyclone without eddy–wind interaction, the difference in tracer concentration was negligible throughout the model run. In the cyclone with eddy–wind interaction, the percent difference increased throughout the simulation.

The analytic model presented in Section 3.2 provides an explicit prediction for the initial rate of accumulation (Equation 12). For a Gaussian eddy with maximum velocity consistent with day 1 of the numerical simulation (0.2316 $\mathrm{m\,s^{-1}}$), the predicted rate was 0.58% per day. The initial rate of concentration in the "$\tau(U_w - u_s)$" simulation was 0.50% per day (Figure 7b). For the "strong" case, the predicted rate was 0.93% per day and initial rate in the simulation was 1.1% per day. The agreement between the analytic model and the early part of the numerical simulation suggests the underlying conceptual model of accumulation is correct.

The rate of change of tracer concentration in the numerical model slowed over time (Figure 7a) due to a combination of factors. In part, it could be explained by the decaying eddy velocities, which were accompanied by a reduction in the divergent component of the

Ekman transport. As discussed by *Dewar and Flierl* [1987], the eddy–wind interaction mechanism ("top drag") contributes to eddy decay. Total kinetic energy decayed over time in all simulations (Auxiliary Material, Figure A.2). However, in the simulations including the eddy–wind interaction mechanism, the rate of decay was more than four times as rapid as in the simulation without eddy–wind interaction.

Another mechanism leading to slowing of the rate of accumulation of tracer was down-gradient diffusive flux, which increases as tracer gradients grow. Accounting for down-gradient diffusive flux of tracer due to unresolved turbulent eddies, the equation governing tracer concentration along a Lagrangian trajectory (Section 3.2) becomes

$$\frac{1}{C}\frac{DC}{Dt} = -\nabla \cdot \mathbf{u_E} - \frac{1}{C} A_H \nabla^2 C, \tag{13}$$

where A_H is a coefficient used to parameterize horizontal mixing. Along a trajectory, changing tracer concentration is controlled by horizontal divergence of the velocity field, producing gradients in tracer concentration, and diffusive processes, smoothing those gradients. The importance of the diffusive flux term ($\frac{1}{C} A_H \nabla^2 C$) was evaluated by comparison with the convergence of the velocity field ($-\nabla \cdot \mathbf{u_E}$). Based on the analytical velocity field, the maximum contribution by convergence was 9.9×10^{-8} s^{-1}. We estimated the diffusive flux based on the difference in tracer between the eddy center and a distance of approximately $2R$, or about 100 km. We used a diffusivity of $A_H = 200$ m^2 s^{-1} at a scale of 100 km, based on *Okubo* [1971]. This was an "effective" diffusivity representing sub–eddy-scale turbulent transports. The approximate compensating contribution by diffusive processes based on the tracer field in the numerical solution was -9.2×10^{-9} s^{-1} on day 55 of the simulation and -1.9×10^{-8} s^{-1} on day 180. Based on the reduction in maximum geostrophic velocities, the peak convergence would have fallen to 7.3×10^{-8} s^{-1} on day 55

and 3.9×10^{-8} s^{-1} on day 180. Thus the estimated impacts of diffusion increase over time to nearly 50% of the peak convergence based on the idealized velocity field. Over time, eddy velocities decay, leading to a decrease in the magnitude of the convergence, while the diffusive flux increases with the tracer gradient.

On longer timescales, trajectories crossing into the center of the eddy might eventually carry less tracer if they originated far enough from the eddy center due to dilution of tracer in regions of divergence on the northern and southern edges of the eddy (Figure 4a). However, integrating tracer concentration along trajectories using the analytical model (Equations 8, 9, and 13), in the absence of diffusive effects, suggested this effect would not become evident until after about 140 days, near the end of these simulations.

Under the influence of eddy–wind interaction, tracer concentrations increased by 54% at the center of the cyclonic eddy over the course of the 6 month simulation, for the basic case ("$\tau(U_w - u_s)$"), compared to a negligible difference in concentration at the end of the run without eddy–wind interaction ("$\tau(U_w)$") (Table 3). Additional simulations addressed the sensitivity of this result to uncertain parameters in the model. Analysis of sea level anomaly fields over time suggested that OC469 Eddy C3 may have been approximately 1.6 times stronger several months prior to sampling. Amplification of the eddy signal by that factor ("strong") increased the tracer concentration effect to 89% over the 6 month simulation. A factor of 10 increase in floating velocity ("w100") increased the ultimate change in concentration to 76%, while a factor of 10 decrease in floating velocity only decreased the concentration change to 52%.

3.3.3. Comparison with Observations

In order to compare the amplitude of the increase in the model with observations, we estimated the percent difference in integrated colony abundance within C3 from background levels (Table 4). The abundance inside C3, estimated based on the four 11-km bins of VPR track closest to the eddy center, was approximately 1.27×10^4 colonies m^{-2}. In the observations, the assessment of a background level of integrated *Trichodesmium* abundance was not as straightforward. We therefore estimated it in several different ways. First, we computed the average abundance over the segment of VPR track beginning near the center of C3 to the point on the track within A3 with the highest sea level anomaly, as interpolated in time and space from objectively analyzed fields (C3 to A3, Table 4). This background estimate, combined with the mean abundance inside C3, corresponds to a percent increase of 153% within the cyclone. This is higher than the 111% increase that might be anticipated in a numerical simulation in which the "strong" case were combined with high floating velocity, under the assumption that the increase in tracer accumulation due to those modifications would add linearly. However, the C3 to A3 background estimate may be skewed low due to the greater track length sampled within A3 compared to C3. Therefore, we also estimated background abundance as the average of the mean integrated abundances within C3 and A3, where the abundance within A3 was calculated based on the seven 11-km VPR track points nearest the eddy center. This corresponds to an increase of 87.6% within the cyclone, comparable to the level of accumulation at the end of 6 months in the "strong" simulation. We also estimated background abundances based on data compiled by *Luo et al.* [2012] collected between the months of August and December of all years and in the region from 20°N–29°N and 70°W–59°W ("climatology", Table 4, Figure A.3). We chose that region, which is centered to the north of the C3 and

A3 sampling site, taking into account the observed patterns in integrated *Trichodesmium* abundance. Abundance in the *Luo et al.* [2012] climatology increased significantly to the south of the C3 and A3 site, a pattern likely attributable to freshwater influence (see Section 4), which was minimal in the vicinity of C3 and A3. The percent increase relative to the arithmetic mean of the selected data was 59.2%, and the increase was 107% compared to the geometric mean. The former level is reached by the basic "$\tau(U_w - u_s)$" case, and the latter by the "strong" case.

3.4. Discussion

Through idealized eddy simulations based on a three-dimensional primitive equation model, we have shown that Ekman transport convergence due to the influence of eddy velocities on the wind stress field can lead to increased buoyant tracer concentration in cyclonic eddies, consistent with fall 2010 observations of greater *Trichodesmium* abundance in cyclonic eddies. Convergence in cyclones can concentrate buoyant particles such as *Trichodesmium* colonies over periods of several months.

The estimated accumulation rate was specific to the conditions simulated and was likely different from the actual accumulation rate. One source of uncertainty is the colony floating velocity, which has been observed to have large variability in the natural environment. We investigated the sensitivity of the results to 10-fold increase and decrease in tracer floating velocity. The accumulation rate increased markedly in the run with increased floating velocity but was not nearly as sensitive to a decrease in floating velocity. This suggests that the factor controlling the accumulation rate is the vertical location of the tracer relative to the sheared velocity structure. An increase in floating velocity skews the vertical tracer distribution higher in the water column (Figure 6), where inward velocities

are strongest. A decrease has only a small effect on the vertical tracer distribution and therefore on the rate and direction of transport.

Physical factors that may influence accumulation rates associated with eddy–wind interaction include eddy velocities, wind speed, and diurnal heating/cooling. We initialized the model runs with the physical characteristics of the eddy after the pattern in *Trichodesmium* abundance was already present, which would correspond to the end of the simulation. Based on the eddy decay in the simulation, at an earlier time the observed eddies may have had stronger sea level anomalies and azimuthal velocities. These larger velocities would be associated with greater convergence and colony accumulation rate. A model run at greater eddy strength led to a roughly proportional increase in accumulation rate, consistent with the idealized model discussed in Section 3.2. The factor of 1.6 increase produced levels of concentration consistent with the our moderate observation-based estimates.

Quantitatively, there was overlap between the concentration levels reached during the six-month simulations and those estimated based on observations of the region near Eddy C3 in fall 2010. However, the upper range of the observation-based estimates was higher than simulated levels and unlikely to be achieved by the modeled process alone. Some differences between our idealized model and observations are to be expected given the simplified nature of the model, which is not intended to reproduce the full complexity of the natural environment. In addition to wind-driven concentration, spatial heterogeneity in population growth and/or mortality likely contributed to the observed patterns. Many factors can affect net *Trichodesmium* growth rate, such as temperature, salinity, and nutrient availability, as well as mortality. Although this study shows that the phys-

ical mechanism proposed herein could contribute a significant portion of the observed enhancement in cyclones, it does not rule out other mechanisms.

An aspect of the observations not fully explained by the wind-driven concentration model was that although puff colonies were more deeply distributed, their abundance was also elevated in cyclones relative to anticyclones on the fall cruise (Figure 2). Wind-driven concentration would not act to concentrate puffs below the Ekman layer. One possibility is that the puff colonies may have been more buoyant at the time they were advected toward the center of the cyclone and then began to sink. *Villareal and Carpenter* [2003] suggest that *Trichodesmium* colonies may employ carbohydrate ballasting to mine phosphorus at the nutricline. Thus, if the colonies became nutrient stressed when trapped in the convergent cyclone center, the phosphorus mining mechanism could be triggered. The domed isopycnals in cyclones could facilitate this phosphorus acquisition strategy since the phosphocline might be uplifted at the center of the eddy. It is unclear whether puffs and rafts would be affected by nutrient stress at different rates, but rafts are generally observed to be more buoyant and located higher in the water column [*Post et al.*, 2002; *Walsby*, 1978]. Another mechanism that could explain this pattern is exchange between the puff and raft morphology pools. This could occur if raft-shaped colonies were able to transition to a puff shape or if reproduction of *Trichodesmium* initially in raft-shaped colonies could result in some puff-shaped colonies. In this scenario, raft colonies would converge in the eddy center near the surface, and transition to or produce puff colonies, which would sink to the observed depths. The details of colony morphology determination and transition are not clear and warrant further investigation.

4. *Trichodesmium* Colonies in Fresh Anticyclones: Observations and Discussion

Two anticyclones, A4 (Station 7, Figure 1) and A5 (Station 10, Figure 1), observed in spring 2011 (OC471) coincided geographically with local peaks in *Trichodesmium* colony abundance (Figure 8). The local correlation between sea level anomaly and integrated *Trichodesmium* abundance was 0.57 ($p<0.01$) in the region designated Section 2 on the spring cruise, extending from 18.3°N, −61.6°W to 13.0°N, −55.6°W (Figure 8). Whereas *Davis and McGillicuddy* [2006] observed elevated colony abundances in warm and salty anticyclones, salinity within these anticyclones was anomalously low. Eddy A5 was strongly stratified, with a fresh lens at the surface. Eddy A4 exhibited a deep mixed layer, with anomalously fresh water evident as deep as 120 m. Locally, abundance patterns were vertically and laterally consistent across morphologies.

Within spring cruise Section 2, integrated *Trichodesmium* colony abundances were anticorrelated with upper water column salinity and positively correlated with surface temperature. The salinity correlation was strongest when based on average salinity over the upper water column (6–100 m; data were available only below 5 m), which took into account the deeply mixed fresh anomaly in Eddy A4 (correlation coefficient=-0.84, $p<0.01$; Figure 9). In contrast, surface temperature (at 6 m), rather than a depth-mean value, correlated strongly with *Trichodesmium* abundance (correlation coefficient=0.76, $p<0.01$; Figure 9). *Rouco Molina et al.* [2014] found similar correlations using a qPCR method to assess *Trichodesmium* abundance, indicating that the relationships are robust with respect to methodological differences (the VPR samples colonies only, whereas qPCR includes both colonies and free trichomes).

Upper water column salinity and near-surface temperature were themselves correlated over Section 2, but less strongly correlated over the cruise as a whole. On the scale of the full spring cruise, integrated *Trichodesmium* abundances reflect patterns in upper water column salinity more closely than temperature (Figure 9). For the entire cruise, the coefficient of correlation of integrated *Trichodesmium* colony abundance with mean upper 100 m salinity was -0.80 ($p<0.01$), whereas the correlation with 6-m temperature dropped to 0.61 ($p<0.01$). The relationship between abundance and salinity identified in the spring 2011 data was also present in much of the fall 2010 data. The only exception from fall cruise was Section 2, which exhibited low abundances and a strong association with cyclonic eddies (Figure 2). This subset of the data populated a distinct region in abundance-salinity space (Figure 9).

Previous studies of Amazon plume dispersal point to advection of fresh riverine water into this region along the path of the North Brazil Current (NBC) [*Coles et al.*, 2013; *Richardson and Reverdin*, 1987]. The NBC retroflection persists through much of the year and sheds rings that carry fresh water emanating from the Amazon River plume to the northwest near the South American continent and toward the Caribbean Sea [*Coles et al.*, 2013; *Hellweger and Gordon*, 2002]. In the absence of the retroflection, Amazon River water is transported along this pathway directly through the continuation of the NBC. Based on $^{228}Ra/^{226}Ra$ ratios sampled in 1981, *Moore et al.* [1986] estimated that 20–30% of surface water near Barbados in May came from the Amazon River estuary.

Plume advection and anticyclonic eddy formation in the North Brazil Current region were evident in operational model hindcasts [*Chassignet et al.*, 2009] from May 2011, when A4 and A5 were observed; in fact, in the hindcast for the date anticyclone A5

was transected, a large, fresh anticyclone was present at the same location (Figure 10). Based on objectively analyzed sea level anomaly fields for the period prior to sampling, anticyclone A5 was one of several rings to have been shed into this region from the North Brazil Current (NBC) in spring 2011. Anticyclone A4 may have evolved from remnants of a preceding ring. Its location and history were consistent with a tendency for North Brazil Current rings to deflect northward upon interaction with the Lesser Antilles reported by *Fratantoni and Richardson* [2006]. Together, these lines of evidence suggested that the anomalously fresh water encountered in A5 and possibly A4 originated in the Amazon River plume.

Amazon river outflow has been previously investigated as a source of nutrients to the Atlantic. Elevated dissolved iron concentrations have been observed in the Amazon River plume [*Bergquist and Boyle*, 2006; *Tovar-Sanchez and Sañudo-Wilhelmy*, 2011; *Subramaniam et al.*, 2008] as well as in a fresh eddy with chemical characteristics typical of Amazon plume water [*Fitzsimmons et al.*, 2013]. Elevated phosphorus has likewise been observed in the plume [*Tovar-Sanchez and Sañudo-Wilhelmy*, 2011; *Sohm and Capone*, 2010; *Subramaniam et al.*, 2008], particularly the SRP and particular organic phosphorus fractions. *Demaster and Pope* [1996] calculated an intercept of approximately 0.14 μM phosphate at zero nitrate in Amazon shelf waters. At mixing ratios consistent with observed salinities and phosphorus content of 1.10 nmol P colony^{-1} [*Sañudo-Wilhelmy et al.*, 2001], this represents more than enough phosphorus to support observed *Trichodesmium* colony abundances.

Phosphorus and iron, the two nutrients believed to be limiting to *Trichodesmium* growth in the tropical and subtropical Atlantic, have thus been demonstrated to be supplied

though freshwater of riverine origin, and Amazon outflow has been suggested as a nutrient source to *Trichodesmium* [*Coles et al.*, 2004]. We therefore investigated the relationship between salinity and phosphorus in the spring 2011 data to determine if there was evidence of nutrient supply associated with the fresh water that might explain the observed patterns in *Trichodesmium* abundance (Figure 11). Iron concentrations were not measured in the present study.

Integrated *Trichodesmium* colony abundance from microscopic enumeration at stations (presented in terms of approximate phosphorus content in Figure 11a) decreased with increasing mean upper water column salinity (correlation coefficient = 0.94, $p<0.01$), confirming the VPR results. Phosphate measurements from the same stations at which abundance estimates were made (Figure 11b) did not reveal a point-by-point correlation between phosphate concentration and salinity in the upper water column. *Rouco Molina et al.* [2014] did not find a correlation between phosphate and salinity either, although their analysis was based on a different subset of stations.

Phosphate levels at low salinities (<35) were typically at or slightly above the mean for each sampling depth in the upper 40 m. The exception was Station 16 (not shown), which had very low surface salinity and surface phosphate below the limit of detection. This station was located at the very edge of the freshwater lens and therefore may represent a distinct ecological and chemical environment. At some low salinity stations, the amount of phosphorus estimated to be present in the form of *Trichodesmium* colonies was comparable to the observed phosphate concentrations (Figure 11b), whereas the ratio of *Trichodesmium* phosphorus to environmental phosphate at higher salinities was lower. This is consistent with a scenario in which the fresh water was a source of phosphorus to

Trichodesmium, but the phosphorus concentrations have already been drawn down and incorporated into biomass.

Trichodesmium alkaline phosphatase activity (APA) was elevated in low salinity waters, (Figure 11d), although the correlation was not significant at the 95% confidence level (correlation coefficient = -0.30, p=0.12). Stations with elevated APA spanned the range of observed surface phosphate concentrations. Although the *Trichodesmium* alkaline phosphatase gene is regulated by P [*Orchard et al.*, 2009], the enzyme activity has not been strongly correlated to phosphate concentration in this region [*Orchard et al.*, 2010]. This is likely in part due to the APA associated with epibionts [*Van Mooy et al.*, 2012]. Regardless, the presence of elevated activity associated with the low salinity waters is permissive of dissolved organic phosphorus (DOP) hydrolysis [*Dyhrman et al.*, 2006; *Orchard et al.*, 2010], which may be rapidly assimilated.

Although the data did not demonstrate a strong relationship between phosphorus and salinity at locations in the upper water column where *Trichodesmium* colonies were observed, 100-m depth-integrated total dissolved phosphorus (TDP) concentrations were higher at lower mean salinities (Figure 11c). In part, the tendency for elevated 100-m integrated TDP at lower salinity may be explained by a shallowing of the phosphocline to the South, in the same region mean 100-m salinity decreased due to the surface lens. However, the relationship is stronger in TDP than phosphate (not shown), highlighting the importance of the organic pool. Taken together, these data suggest that DOP may be an important nutrient source to *Trichodesmium* populations in low salinity waters, exerting influence over their distribution.

Subramaniam et al. [2008] and *Goes et al.* [2014] described a succession of phytoplankton functional groups downstream in the Amazon River plume. Coastal diatom species dominated until combined N was drawn down, followed by diatom diazotroph associations until Si and soluble reactive phosphorus were drawn down, with *Trichodesmium* further downstream. A key difference between the present study and findings reported by*Foster et al.* [2007], *Goes et al.* [2014], and *Subramaniam et al.* [2008] is that they found higher *Trichodesmium* abundances at "oceanic" (SSS>35) stations compared to "mesohaline" (30<SSS<35) stations, with most of the elevated nitrogen fixation signal at "mesohaline" stations attributed to diatom-diazotroph associations. In contrast, the greatest *Trichodesmium* abundances in the present study were encountered at stations that would be classified as "mesohaline", with a significant ($p<0.01$) correlation between *Trichodesmium* abundance and salinity. The observations discussed by *Foster et al.* [2007], which were also included in the *Subramaniam et al.* [2008] analysis, were made over an area extending from the southern edge of the region sampled in the present study nearly to approximately 5°N, thus closer to the Amazon delta. In addition to this regional difference, although the observations were made at approximately the same time over year, the *Foster et al.* [2007] observations coincided with bloom period for the *Hemiaulus hackie-Richelia* diatom diazotroph association. That elevated *Trichodesmium* abundances were associated with fresh water influence in the present study suggests that Si may be drawn down before oceanic salinities are reached, and advected river plume water may continue to supply phosphorus and possibly other nutrients necessary for *Trichodesmium* growth.

The supply of phosphorus and iron through river outflow has led to the hypothesis that *Trichodesmium* growth fed by riverine nutrients and growth-conducive surface stratifica-

tion might seed populations throughout the region. In this context, the present study provides a novel high resolution record of gradients in *Trichodesmium* colony abundance associated with salinity and indications of eddy-associated transport of *Trichodesmium* biomass and nutrients from the Amazon plume region to the southwestern North Atlantic.

5. Conclusions

Two different mesoscale associations between *Trichodesmium* colony abundance and the physical environment were observed in the western tropical North Atlantic. Elevated *Trichodesmium* abundances were attributed to riverine freshwater supply associated with anticyclonic eddies, consistent with the ecological succession described by *Subramaniam et al.* [2008] within river plume waters. Greater colony abundances observed in cyclones were hypothesized to result from concentration through convergent Ekman transport. The potential action of this mechanism was supported by an analytical model and idealized simulations.

The two patterns observed are likely to prevail under very different ecological conditions. In order for the relatively slow physical concentration mechanism to produce observable patterns, spatial variation in population growth must be small. This requirement may be more likely to be met in uniformly low-nutrient, low-growth conditions, possibly with balanced growth and mortality. In contrast, under more dynamic bloom conditions, given *Trichodesmium* doubling times in the range of 2.6–5 days [*Rodier and Borgne*, 2010; *Carpenter et al.*, 1993], relationships with factors influencing growth rate, particularly nutrient availability and temperature dependence, are likely to dominate. Enhancement of *Trichodesmium* abundance due to growth in nutrient-rich, fresh, anticyclonic eddies presumably overcomes the effect of the eddy–wind interaction mechanism, which would

tend to dilute the population due to divergence and associated upwelling in the anticyclone interior.

Previous studies have also identified elevated *Trichodesmium* abundances associated with anticyclonic eddies. *Taboada et al.* [2010] attributed their observations to trapping of *Trichodesmium* biomass in an anticyclonic eddy in the eastern North Atlantic subtropical gyre. The *Fong et al.* [2008], *Davis and McGillicuddy* [2006], and present observations were attributed to nutrient environments conducive to local growth within the eddies: low nitrogen with sufficient phosphorus and iron. However, the environments and mechanisms producing these conditions were different in each case. The *Fong et al.* [2008] observations were of a decaying anticyclone in the North Pacific subtropical gyre. The *Davis and McGillicuddy* [2006] observations of elevated *Trichodesmium* colony abundance in warm and salty anticyclones in the northern limb of the North Atlantic subtropical gyre have recently been attributed to a combination of down-gradient transport of biomass and phosphorus by anticyclones originating in the Gulf Stream [*McGillicuddy*, 2014]. The present study attributes the conditions to nutrient supply through transport of Amazon plume water to the southwestern North Atlantic. All of these findings underscore the importance of physical processes in shaping abundance patterns underlying the processes driving carbon and nitrogen cycling in the world's tropical and subtropical oceans.

We conclude that wind-driven concentration could produce patterns qualitatively consistent with the association of *Trichodesmium* abundance with cyclones, and that freshwater input was the driving factor in the association with anticyclones. Future work, including analysis of wind-driven concentration through more sophisticated and higher resolution models, could further elucidate the relationship between *Trichodesmium* colonies and

their physical environment. Patterns of buoyant tracer imbedded in a basin-scale eddy-resolving model with a realistic wind field could facilitate assessment of the mechanism in a more realistic simulation.

Acknowledgments. We sincerely thank the officers and crew of the R/V *Oceanus* as well as the science participants. M. Oates assisted with VPR image classification. H. Joy-Warren completed the microscopic enumeration of colonies. A. Heithoff and M. Rouco participated in collection and analysis of nutrient data. Toby Westberry provided ocean-color-based estimates of *Trichodesmium* bloom probability during the two cruises. Altimeter products were produced and distributed by AVISO (www.aviso.oceanobs.com/) as part of the Ssalto ground processing segment. V. Kosnyrev assisted in the analysis of altimetric data. L. Anderson provided guidance and support for setting up POP model runs. Computing resources (ark:/85065/d7wd3xhc) were provided by the Climate Simulation Laboratory at NCAR's Computational and Information Systems Laboratory, sponsored by the National Science Foundation and other agencies. We gratefully acknowledge support of this research by NSF and NASA. A NASA Earth and Space Science Fellowship supported E. Olson's graduate studies.

References

Antonov, J. I., D. Seidov, T. P. Boyer, R. A. Locarnini, A. V. Mishonov, H. E. Garcia, O. K. Baranova, M. M. Zweng, and D. R. Johnson (2010), *World Ocean Atlas 2009, Volume 2: Salinity*, p. 184, NOAA Atlas NESDIS 69, U.S. Government Printing Office, Washington, D.C.

Bar-Zeev, E., I. Avishay, K. D. Bidle, and I. Berman-Frank (2013), Programmed cell death in the marine cyanobacterium *Trichodesmium* mediates carbon and nitrogen export, *The ISME Journal*, *7*, 2340–2348, doi:10.1038/ismej.2013.121.

Batchelor, G. K. (1967), *An Introduction to Fluid Dynamics*, 2000 ed., Cambridge University Press.

Bergquist, B. A., and E. A. Boyle (2006), Iron isotopes in the Amazon River system: Weathering and transport signatures, *Earth and Planetary Science Letters*, *248*, 54–68, doi:10.1016/j.epsl.2006.05.004.

Capone, D. G., J. P. Zehr, H. W. Paerl, B. Bergman, and E. J. Carpenter (1997), *Trichodesmium*, a globally significant marine cyanobacterium, *Science*, *276*, 1221–1229.

Capone, D. G., A. Subramaniam, J. P. Montoya, M. Voss, C. Humborg, A. M. Johansen, R. L. Siefert, and E. J. Carpenter (1998), An extensive bloom of the N_2-fixing cyanobacterium *Trichodesmium erythraeum* in the central Arabian Sea, *Marine Ecology Progress Series*, *172*, 281–292.

Carpenter, E. J. (1983), Physiology and ecology of marine planktonic *Oscillatoria (Trichodesmium)*, *Marine Biology Letters*, *4*(2), 69–85.

Carpenter, E. J., J. M. O'Neil, R. Dawson, D. G. Capone, P. J. A. Siddiqui, T. Roenneberg, and B. Bergman (1993), The tropical diazotrophic phytoplankter *Trichodesmium*: biological characteristics of two common species, *Marine Ecology Progress Series*, *95*, 295–304.

Chassignet, E., H. Hurlburt, E. Metzger, O. Smedstad, J. Cummings, G. Halliwell, R. Bleck, R. Baraille, A. Wallcraft, C. Lozano, H. Tolman, A. Srinivasan, S. Hankin, P. Cornillon, R. Weisberg, A. Barth, R. He, F. Werner, and J. Wilkin (2009), U.s.

godae: Global ocean prediction with the hybrid coordinate ocean model (HYCOM), *Oceanography*, *22*(2), 64–75.

Coles, V. J., C. Wilson, and R. R. Hood (2004), Remote sensing of new production fueled by nitrogen fixation, *Geophysical Research Letters*, *31*, L06,301, doi: 10.1029/2003GL019018.

Coles, V. J., M. T. Brooks, J. Hopkins, M. R. Stukel, P. L. Yager, and R. R. Hood (2013), The pathways and properties of the amazon river plume in the tropical north atlantic ocean, *Journal of Geophysical Research: Oceans*, *118*, 6894–6913.

Davis, C. S., and D. J. McGillicuddy (2006), Transatlantic abundance of the N_2-fixing colonial cyanobacterium *Trichodesmium*, *Science*, *312*(5779), 1517 – 1520, doi: 10.1126/science.1123570.

Davis, C. S., F. T. Thwaites, S. M. Gallager, and Q. Hu (2005), A three-axis fast-tow digital video plankton recorder for rapid surveys of plankton taxa and hydrography, *Limnology and Oceanography Methods*, *3*, 59–74.

Demaster, D. J., and R. H. Pope (1996), Nutrient dynamics in Amazon shelf waters: results from AMASSEDS, *Continental Shelf Research*, *16*(3), 263–289.

Dewar, W. K., and G. R. Flierl (1987), Some effects of the wind on rings, *Journal of Physical Oceanography*, *17*(10), 1653–1667.

Dore, J. E., J. R. Brum, L. M. Tupas, and D. M. Karl (2002), Seasonal and interannual variability in sources of nitrogen supporting export in the oligotrophic subtropical North Pacific Ocean, *Limnology and Oceanography*, *47*(6), 1595–1607.

Dyhrman, S. T., and K. C. Ruttenberg (2006), Presence and regulation of alkaline phosphatase activity in eukaryotic phytoplankton from the coastal ocean: Implications for

dissolved organic phosphorus remineralization, *Limnology and Oceanography*, *51*(3), 1381–1390.

Dyhrman, S. T., P. D. Chappell, S. T. Haley, J. W. Moffett, E. D. Orchard, J. B. Waterbury, and E. A. Webb (2006), Phosphonate utilization by the globally important marine diazotroph *Trichodesmium*, *Nature*, *439*, 68–71.

Falkowski, P. G., D. Ziemann, Z. Kolber, and P. K. Bienfang (1991), Role of eddy pumping in enhancing primary production in the ocean, *Nature*, *352*, 55–58.

Fitzsimmons, J. N., R. Zhang, and E. A. Boyle (2013), Dissolved iron in the tropical North Atlantic Ocean, *Marine Chemistry*, *154*, 87–99, doi:10.1016/j.marchem.2013.05.009.

Fong, A. A., D. M. Karl, R. Lukas, R. M. Letelier, J. P. Zehr, and M. J. Church (2008), Nitrogen fixation in an anticyclonic eddy in the oligotrophic North Pacific Ocean, *The ISME Journal*, *2*, 663–676.

Foster, R. A., A. Subramaniam, C. Mahaffey, E. J. Carpenter, D. G. Capone, and J. P. Zehr (2007), Influence of the Amazon River plume on distributions of free-living and symbiotic cyanobacteria in the western tropical North Atlantic Ocean, *Limnology and Oceanography*, *52*(2), 517–532.

Franks, P. J. S. (1992), Sink or swim: accumulation of biomass at fronts, *Marine Ecology Progress Series*, *82*(1), 1–12.

Fratantoni, D. M., and P. L. Richardson (2006), The evolution and demise of North Brazil Current rings, *Journal of Physical Oceanography*, *36*, 1241–1264.

Goes, J. I., H. do Rosario Gomes, A. M. Chekalyuk, E. J. Carpenter, J. P. Montoya, V. J. Coles, P. L. Yager, W. M. Berelson, D. G. Capone, R. A. Foster, D. K. Steinberg, A. Subramaniam, and M. A. Hafez (2014), Influence of the Amazon River discharge on

the biogeography of phytoplankton communities in the western tropical North Atlantic, *Progress in Oceanography*, *120*, 29–40, doi:10.1016/j.pocean.2013.07.010.

Hellweger, F. L., and A. L. Gordon (2002), Tracing Amazon River water into the Caribbean Sea, *Journal of Marine Research*, *60*, 537–549.

Hu, Q., and C. Davis (2006), Accurate automatic quantification of taxa-specific plankton abundance using dual classification with correction, *Marine Ecology Progress Series*, *306*, 51–61.

LaRoche, J., and E. Breitbarth (2005), Importance of the diazotrophs as a source of new nitrogen in the ocean, *Journal of Sea Research*, *53*, 57–91, doi: 10.1016/j.seares.2004.05.005.

Ledwell, J. R., D. J. McGillicuddy, and L. A. Anderson (2008), Nutrient flux into an intense deep chlorophyll layer in a mode-water eddy, *Deep Sea Research Part II: Topical Studies in Oceanography*, *55*, 1139–1160, doi:10.1016/j.dsr2.2008.02.005.

Letelier, R. M., and D. M. Karl (1996), Role of *Trichodesmium* spp. in the productivity of the subtropical North Pacific Ocean, *Marine Ecology Progress Series*, *133*, 263–273.

Locarnini, R. A., A. V. Mishonov, J. I. Antonov, T. P. Boyer, H. E. Garcia, O. K. Baranova, M. M. Zweng, and D. R. Johnson (2010), *World Ocean Atlas 2009, Volume 1: Temperature*, p. 184, NOAA Atlas NESDIS 69, U.S. Government Printing Office, Washington, D.C.

Luo, Y.-W., S. C. Doney, L. A. Anderson, M. Benavides, I. Berman-Frank, A. Bode, S. Bonnet, K. H. Boström, D. Böttjer, D. G. Capone, E. J. Carpenter, Y. L. Chen, M. J. Church, J. E. Dore, L. I. Falcón, A. Fernández, R. A. Foster, K. Furuya, F. Gómez, K. Gundersen, A. M. Hynes, K. M. Karl, S. Kitajima, R. J. Langlois, J. LaRoche,

R. M. L. E. Marañón, D. J. McGillicuddy, P. H. Moisander, C. M. Moore, B. Mouriño-Carballido, M. R. Mulholland, J. A. Needoba, K. M. Orcutt, A. J. P. E. Rahav, P. Raimbault, A. P. Rees, L. Riemann, T. Shiozaki, A. Subramaniam, T. Tyrrell, K. A. Turk-Kubo, M. Varela, T. A. Villareal, E. A. Webb, A. E. White, J. Wu, and J. Zehr (2012), Database of diazotrophs in global ocean: abundance, biomass and nitrogen fixation rates, *Earth Syst. Sci. Data*, *4*, 47–73.

Martin, A. P., and K. J. Richards (2001), Mechanisms for vertical nutrient transport within a North Atlantic mesoscale eddy, *Deep-Sea Research II*, *48*, 757–773.

McGillicuddy, D. J. (2014), Do *Trichodesmium* spp. populations in the North Atlantic export most of the nitrogen they fix?, *Global Biogeochemical Cycles*, *28*, doi: 10.1002/2013GB004652.

McGillicuddy, D. J., and A. R. Robinson (1997), Eddy-induced nutrient supply and new production in the Sargasso Sea, *Deep-Sea Research I*, *44*(8), 1427–1450.

McGillicuddy, D. J., L. Anderson, N. Bates, T. Bibby, K. Buesseler, C. Carlson, C. Davis, C. Ewart, P. Falkowski, S. Goldthwait, D. Hansell, W. Jenkins, R. Johnson, V. Kosnyrev, J. Ledwell, Q. Li, D. Siegel, and D. Steinberg (2007), Eddy/wind interactions stimulate extraordinary mid-ocean plankton blooms, *Science*, *316*, 1021–1026, doi: 10.1126/science.1136256.

Moore, W. S., J. L. Sarmiento, and R. M. Key (1986), Tracing the Amazon component of surface Atlantic water using ^{228}Ra, salinity and silica, *Journal of Geophysical Research*, *91*(C2), 2574–2580.

Okubo, A. (1971), Oceanic diffusion diagrams, *Deep-Sea Research*, *18*, 789–802.

Olson, E. M. (2014), Investigating the role of *Trichodesmium* spp. in the oceanic nitrogen cycle through observations and models, Ph.D. thesis, Massachusetts Institute of Technology and the Woods Hole Oceanographic Institution.

Orchard, E. D., E. A. Webb, and S. T. Dyhrman (2009), Molecular analysis of the phosphorus starvation response in *Trichodesmium* spp., *Environmental Microbiology*, *11*(9), 2400–2411, doi:10.1111/j.1462-2920.2009.01968.x.

Orchard, E. D., J. W. Ammerman, M. W. Lomas, and S. T. Dyhrman (2010), Dissolved inorganic and organic phosphorus uptake in *Trichodesmium* and the microbial community: The importance of phosphorus ester in the Sargasso Sea, *Limnology and Oceanography*, *55*(3), 1390–1399.

Post, A. F., Z. Dedej, R. Gottlieb, H. Li, D. N. Thomas, M. El-Absawi, A. El-Naggar, M. El-Gharabawi, and U. Sommer (2002), Spatial and temporal distribution of *Trichodesmium* spp. in the stratified Gulf of Aqaba, Red Sea, *Marine Ecology Progress Series*, *239*, 241–250.

Richardson, P. L., and G. Reverdin (1987), Seasonal cycle of velocity in the atlantic north equatorial countercurrent as measured by surface drifters, current meters, and ship drifts, *Journal of Geophysical Research*, *92*(C4), 3691–3708.

Rodier, M., and R. L. Borgne (2010), Population and trophic dynamics of *Trichodesmium thiebautii* in the SE lagoon of new caledonia. Comparison with t. erythraeum in the sw lagoon, *Marine Pollution Bulletin*, *61*, 349–359.

Rouco Molina, M., H. Joy-Warren, D. J. McGillicuddy, J. B. Waterbury, and S. T. Dyhrman (2014), *Trichodesmium* sp. clade distributions in the western North Atlantic, *Limnology and Oceanography.* In press.

Sañudo-Wilhelmy, S. A., A. B. Kustka, C. J. Gobler, D. A. Hutchins, M. Yang, K. Lwiza, J. Burns, D. G. Capone, J. A. Raven, and E. J. Carpenter (2001), Phosphorus limitation of nitrogen fixation by *Trichodesmium* in the central Atlantic Ocean, *Nature*, *441*, 66–69.

Smith, R. D., M. E. Maltrud, F. O. Bryan, and M. W. Hecht (2000), Numerical simulation of the North Atlantic Ocean at 1/10 degree, *Journal of Physical Oceanography*, *30*, 1532–1561.

Sohm, J. A., and D. G. Capone (2010), Zonal differences in phosphorus pools, turnover and deficiency across the tropical North Atlantic Ocean, *Global Biogeochemical Cycles*, *24*, GB2008, doi:10.1029/2008GB003414.

Subramaniam, A., P. L. Yager, E. J. Carpenter, C. Mahaffey, K. Bjoörkman, S. Cooley, A. B. Kustka, J. P. Montoya, S. A. Sañudo-Wilhelmy, R. Shipe, and D. G. Capone (2008), Amazon River enhances diazotrophy and carbon sequestration in the tropical North Atlantic Ocean, *PNAS*, *105*(30), 10,460–10,465.

Taboada, F. G., R. G. Gil, J. Höfer, S. González, and R. Anadón (2010), *Trichodesmium* spp. population structure in the eastern North Atlantic subtropical gyre, *Deep-Sea Research I*, *57*, 65–77.

Tovar-Sanchez, A., and S. A. Sañudo-Wilhelmy (2011), Influence of the Amazon River on dissolved and intra-cellular metal concentrations in *Trichodesmium* colonies along the western boundary of the sub-tropical North Atlantic Ocean, *Biogeosciences*, *8*, 217–225, doi:10.5194/bg-8-217-2011.

Van Mooy, B. A. S., L. R. Hmelo, L. E. Sofen, S. R. Campagna, A. L. May, S. T. Dyhrman, A. Heithoff, E. A. Webb, L. Momper, and T. J. Mincer (2012), Quorum sensing control

of phosphorus acquisition in *Trichodesmium* consortia, *The ISME Journal*, *6*, 422–429, doi:10.1038/ismej.2011.115.

Villareal, T. A., and E. J. Carpenter (2003), Buoyancy regulation and the potential for vertical migration in the oceanic cyanobacterium *Trichodesmium*, *Microbial Ecology*, *45*(1), pp. 1–10.

Walsby, A. (1992), The gas vesicles and buoyancy of *Trichodesmium*, in *Marine Pelagic Cyanobacteria: Trichodesmium and other Diazotrophs*, *NATO ASI Series*, vol. 362, edited by E. Carpenter, D. Capone, and J. Rueter, pp. 141–161, Springer Netherlands.

Walsby, A. E. (1978), The properties and buoyancy-providing role of gas vacuoles in *Trichodesmium ehrenberg*, *Br. Phycol. J.*, *13*, 103–116.

Westberry, T., D. Siegel, and A. Subramaniam (2005), An improved bio-optical model for the remote sensing of *Trichodesmium* spp. blooms, *Journal of Geophysical Research—Oceans*, *110*(C6), doi:10.1029/2004JC002517.

Westberry, T. K., and D. A. Siegel (2006), Spatial and temporal distribution of *Trichodesmium* blooms in the world's oceans, *Global Biogeochemical Cycles*, *20*(4), doi:10.1029/2005GB002673.

Zhong, Y., A. Bracco, and T. A. Villareal (2012), Pattern formation at the ocean surface: Sargassum distribution and the role of the eddy field, *Limnology & Oceanography: Fluids & Environments*, *2*, 12–27.

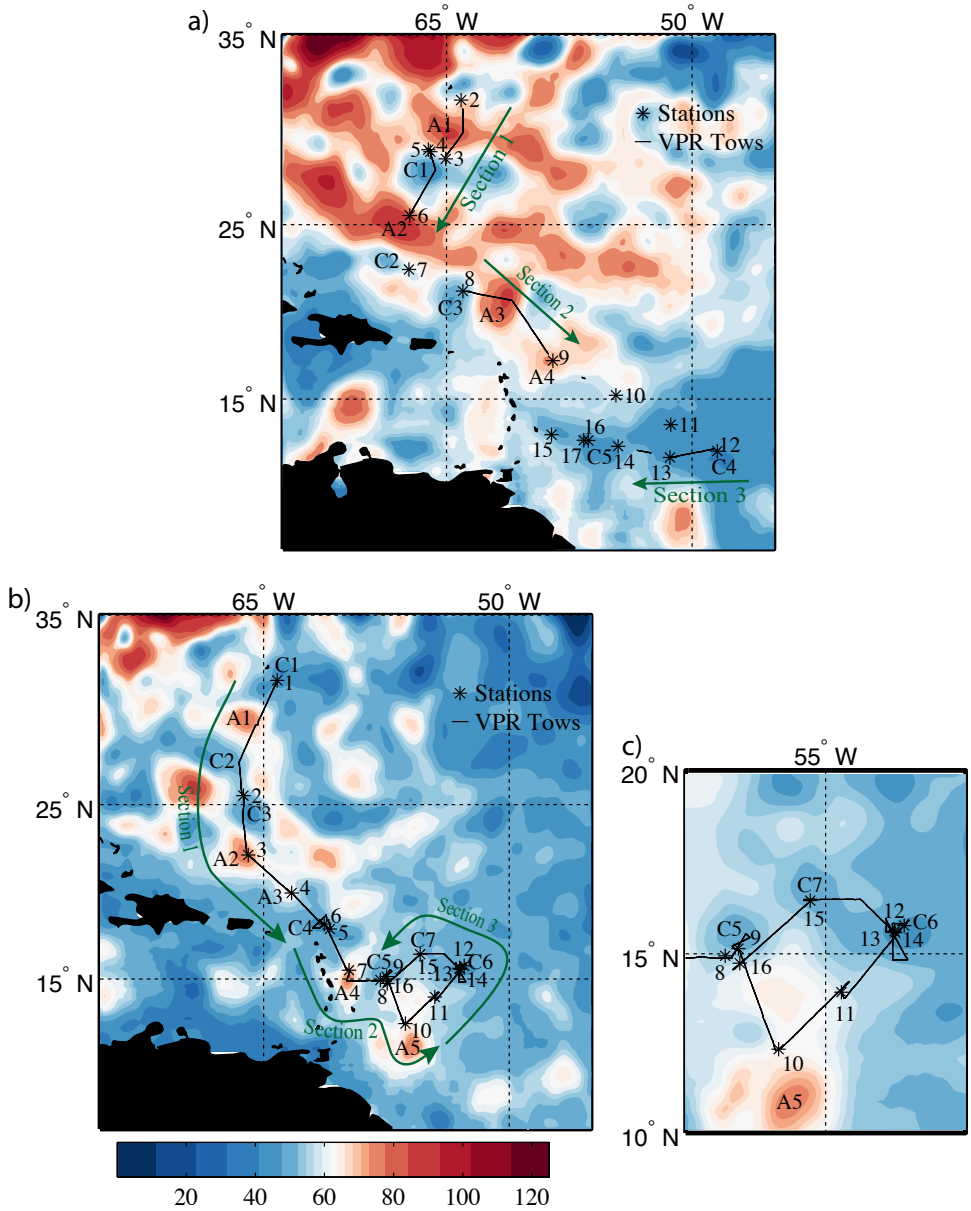

Figure 1. Locations of stations and VPR tows for a) the Fall Cruise and b) the Spring Cruise with absolute dynamic topography (ADT) in cm. Black lines indicate VPR tows. Stars indicate station locations. Targeted cyclonic and anticyclonic eddies are labeled with prefixes "C" and "A", respectively. Labeled sections (arrows) are referred to in subsequent analysis. ADT was calculated by objective analysis of available altimetry data from Envisat and Jason-1/2. c) Southwestern portion of the Spring Cruise track and altimetry magnified and for a later date (May 8, 2011), when cyclone C7 was more apparent.

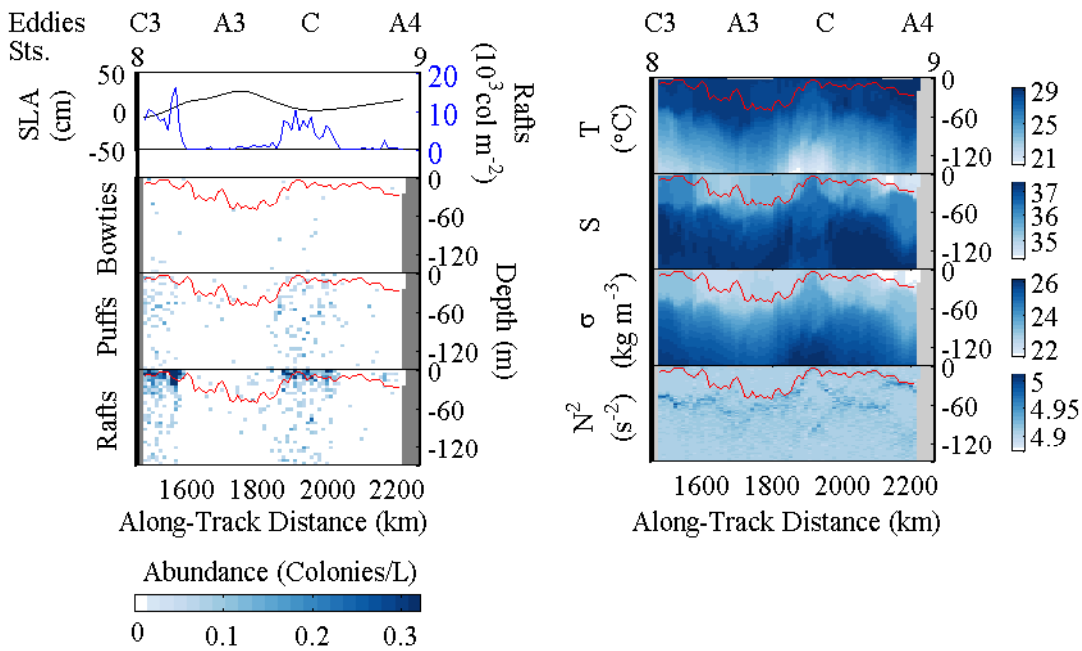

Figure 2. *Trichodesmium* abundance and physical properties associated with eddies transected on section 2 of fall 2010 cruise OC469. Black line in upper panel is sea level anomaly (cm). Blue line in upper panel represents integrated raft colony abundance (10×10^3 colonies m^{-2}). Red lines show mixed layer depth as determined by a threshold criterion of 0.125 kg m^{-3} density difference from the surface. Right panels (top to bottom) display temperature, salinity, density, and buoyancy frequency.

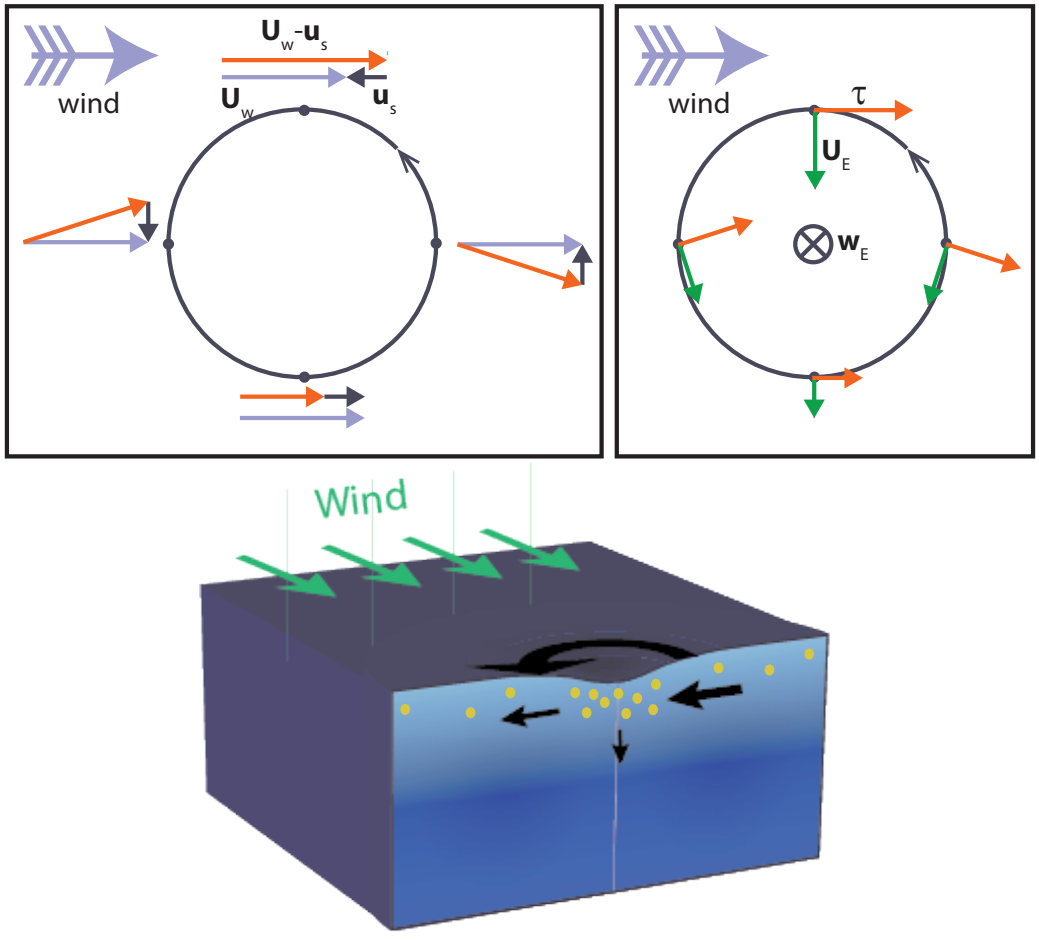

Figure 3. Schematic diagram of Ekman convergence concentration of buoyant colonies in a cyclone with wind stress a function of the difference between air and sea surface velocity ($\tau \propto |U_w - u_s|(U_w - u_s)$). Upper left: plan view of a cyclonic eddy with the difference (black) between wind velocity, U_w (blue), and sea surface velocity, u_s (orange), at four points. Upper right: direction of the resulting wind stress, τ (orange), and Ekman transport, U_E (green), at the same locations. Convergence of Ekman transport near the center of the eddy leads to downwelling, w_E. Lower: buoyant colonies become concentrated in a region of surface convergence and downwelling in the center of a cyclonic eddy with uniform wind.

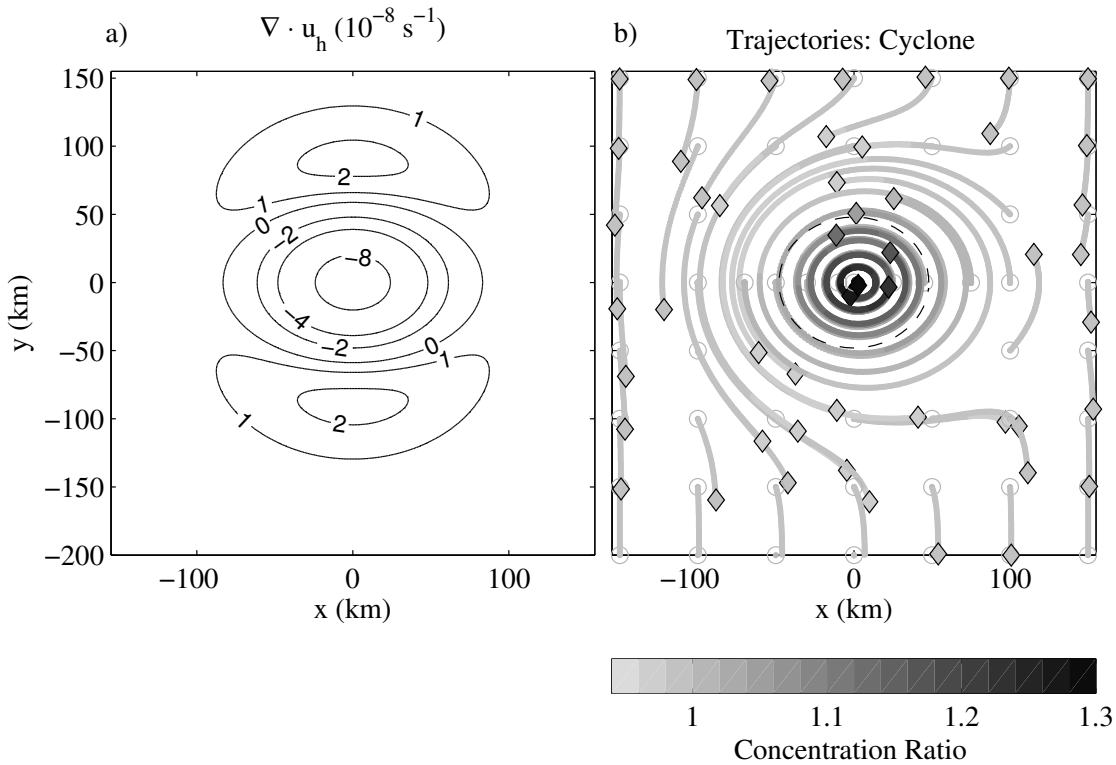

Figure 4. a) Contours of the divergence of the horizontal velocity field (Equations 8 and 9). Flow is convergent near the eddy center, with regions of divergence to the north and south in the presence of a uniform westerly wind. b) 30-day trajectories calculated based on the same horizontal surface boundary layer velocities, which result from a combination of azimuthal eddy velocities and wind-driven Ekman transport. A black dashed line marks the radius of maximum velocity of the eddy at 48 km. A circle represents the point of origin of each trajectory, and a diamond marks the end location. Shading indicates tracer concentration as the ratio of final to initial value along each Lagrangian trajectory. Tracer concentration was calculated by integration of Equation 7, which does not include the effects of down-gradient diffusive flux due to horizontal mixing.

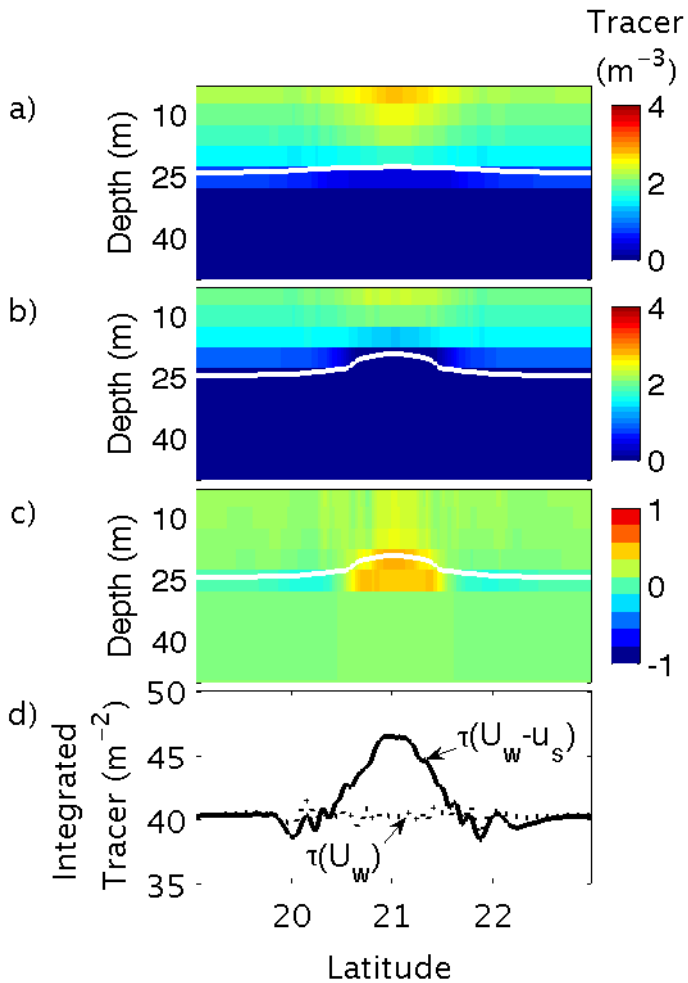

Figure 5. 20-day (Days 12 to 31) mean tracer concentrations. Upper three panels: tracer concentration fields in a cross-section through the eddy center with white contours marking mixed layer depths determined by a 0.025 kg m^{-3} potential density difference from the surface. a) With eddy–wind interaction: $\tau(U_w - u_s)$. b) Without eddy–wind interaction: $\tau(U_w)$. c) Difference between $\tau(U_w - u_s)$ and $\tau(U_w)$. Mixed layer depths are shown in white; the $\tau(U_w)$ mixed layer depth is repeated in panel c. e) Depth-integrated tracer concentration for the model runs with ($\tau(U_w - u_s)$) and without ($\tau(U_w)$) eddy–wind interaction. Solid line: $\tau(U_w - u_s)$. Dashed line: $\tau(U_w)$.

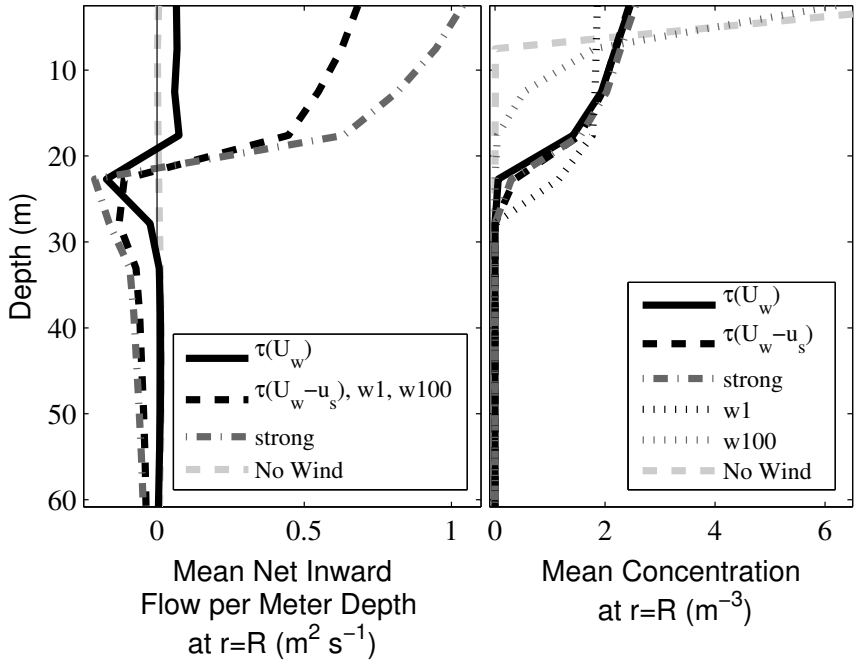

Figure 6. Left: 20-day mean vertical profiles of inward volume transport per meter depth across a circle centered at eddy center with walls at a radius of 48 km, approximately the radius of maximum eddy velocity. Right: 20-day mean vertical profiles of tracer concentration at 48 km from eddy center. Volume transports and concentration profiles are displayed for runs described in Table 2.

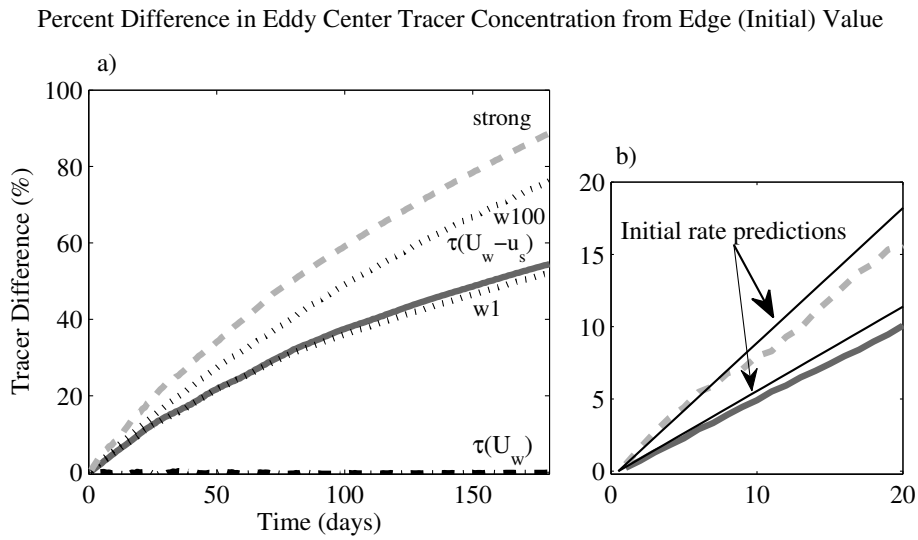

Figure 7. a) Difference in eddy center tracer concentration from initial concentration vs. time. Center concentration is the average depth-integrated tracer concentration within a radius of 48 km of the eddy center. Lines represent various model runs described in Table 2: "$\tau(U_w)$" (gray), "$\tau(U_w - u_s)$" (blue), "w1" (red), "w100" (orange), and "strong" (green). b) Enlarged lower right corner of (a), showing only the "$\tau(U_w - u_s)$" and "strong" cases, which have the eddy–wind interaction turned on and tracer floating velocities of 10 $\mathrm{m\,d^{-1}}$. Black lines represent predictions of initial accumulation rates calculated based on Ekman pumping in idealized eddies (Equation 12 with eddy velocities of $v_\theta = 0.23$ $\mathrm{m\,s^{-1}}$ ($\tau(U_w - u_s)$)and $v_\theta = 0.37$ $\mathrm{m\,s^{-1}}$ ("strong"), representative of model geostrophic azimuthal velocities on simulation day 1.

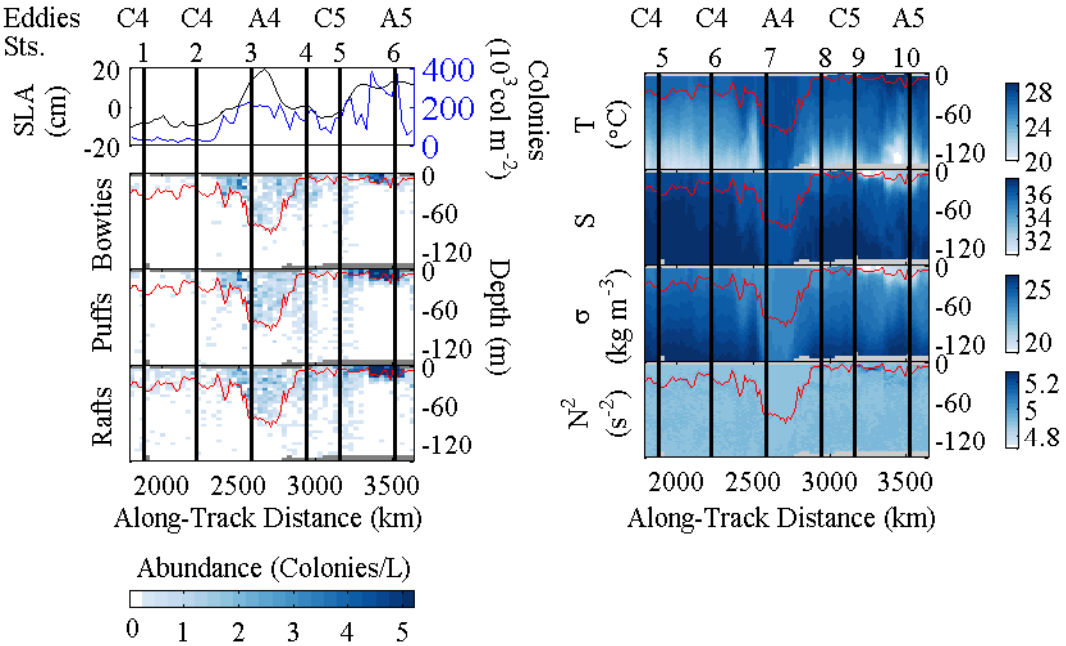

Figure 8. *Trichodesmium* abundance and physical properties associated with eddies transected on spring cruise OC471.

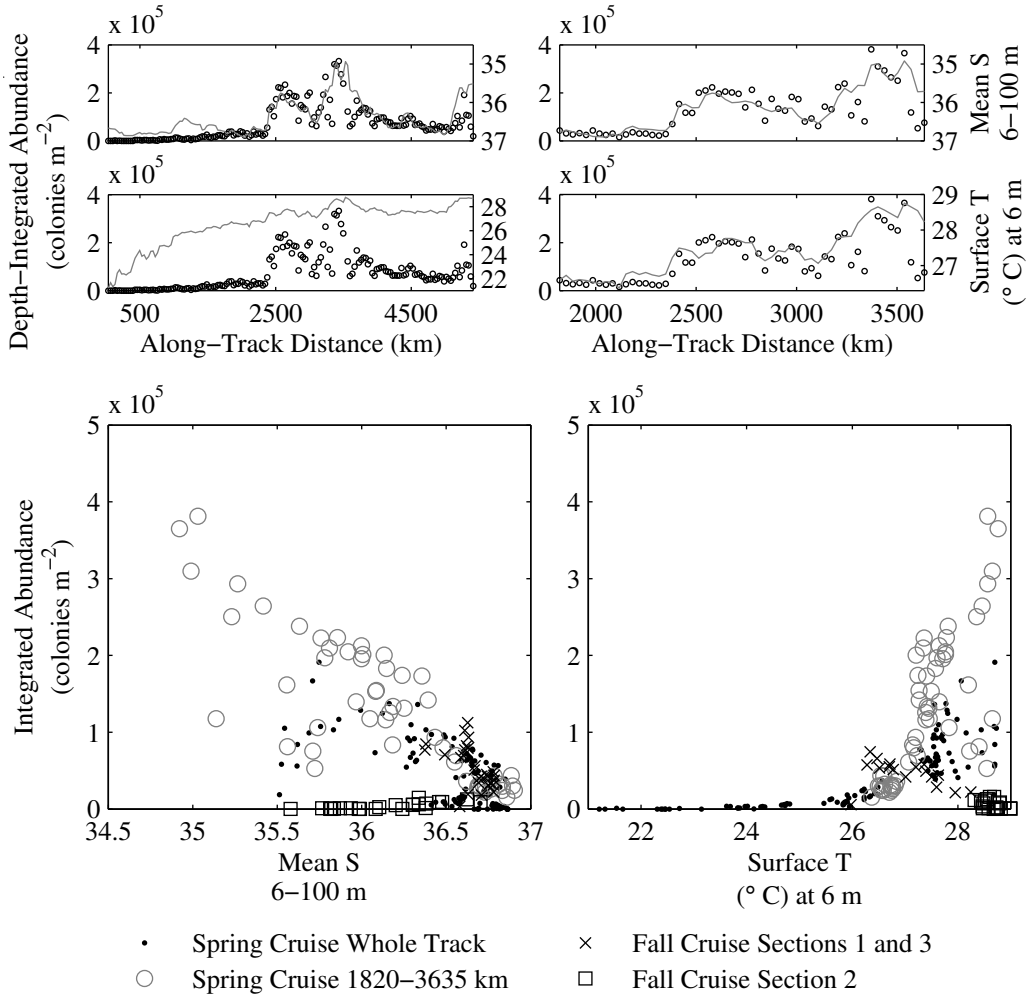

Figure 9. Relationship between depth-integrated *Trichodesmium* abundance and temperature and salinity for the entire spring cruise and for the subset of the spring cruise designated Section 2 and displayed in Figure 8. Upper four panels: Solid line represents salinity (upper) or temperature (middle) and open circles represent *Trichodesmium* colony abundance. Salinity here is the mean over the upper 100 m, whereas temperature is the near-surface value observed at 6 m depth. Note that salinity axes are reversed in the upper panels to emphasize the degree of anticorrelation between mean salinity and depth-integrated *Trichodesmium* abundance. Lower panels: Scatter plots of abundance vs. mean salinity (left) and surface temperature (right). Data from the fall cruise are also included in the scatter plots.

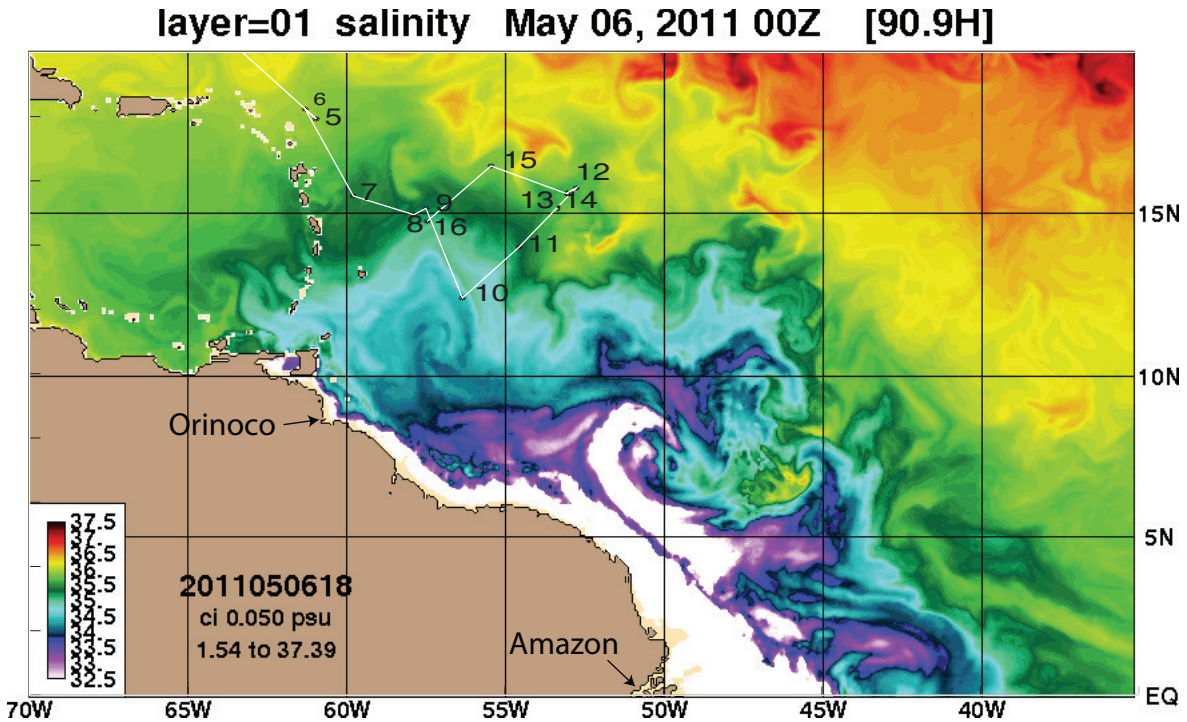

Figure 10. Sea Surface Salinity from Naval Research Laboratory 1/12° Global HYCOM Hindcast (http://www7320.nrlssc.navy.mil/GLBhycom1-12/navo/nbrazlsss/nowcast/sss2011050618_2011050600_909_nbrazlsss.001.gif). Cruise track, station locations, and Orinoco and Amazon River mouths are indicated.

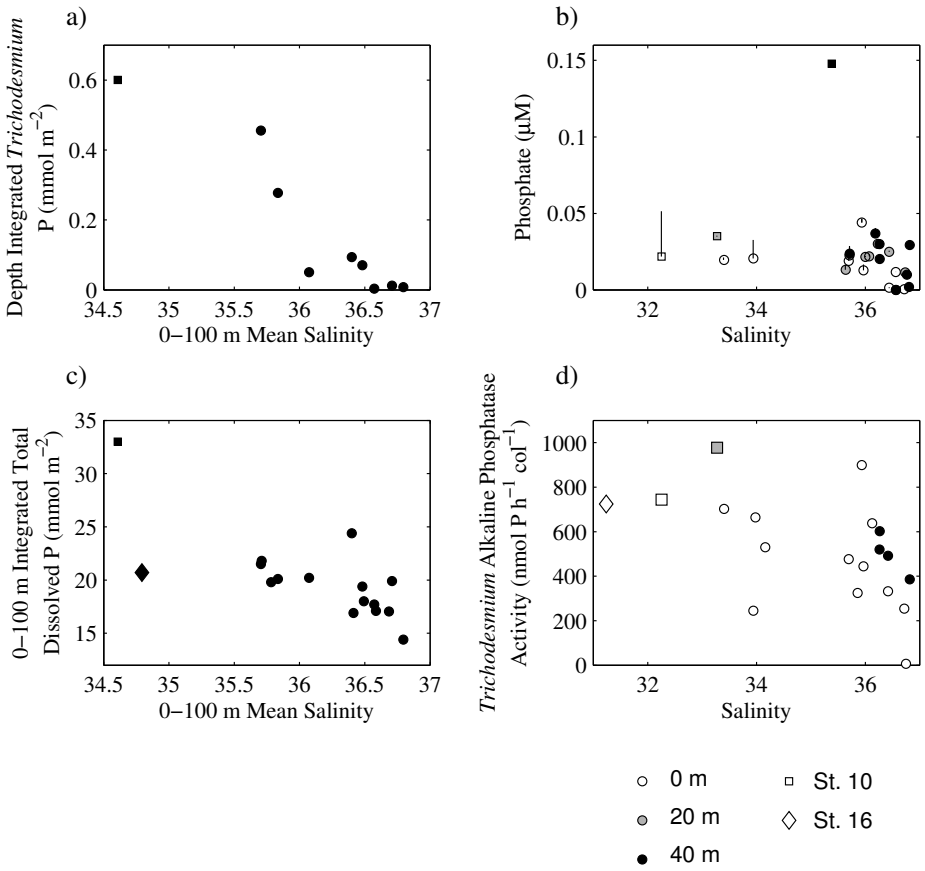

Figure 11. a) Depth-integrated *Trichodesmium* P content vs. upper 100 m mean salinity. P content was estimated from microscopically enumerated colony abundance with conversion factor of 1.10 nmol P per colony [*Sañudo-Wilhelmy et al.*, 2001]. Depth-mean salinitywas calculated by trapezoidal integration of measurements at the 20 m intervals (the resolution of the nutrient data). b) Phosphate concentration vs. salinity at matched depths for stations with *Trichodesmium* colony abundance data from microscopic enumeration. Lines extending upward from data points represent the estimated P content of *Trichodesmium* colonies at that depth. c) Total dissolved phosphorus content, by trapezoidal integration from the surface to 100 m, vs. mean salinity based on the same 20-m sampling resolution. d) *Trichodesmium* alkaline phosphatase activity vs. salinity. Samples matched to 0 m salinity were actually taken from net tows at 5 m depth. For panels b) and d), symbol shading indicates sample depth and symbol shape is used to identify data from two stations, 10 and 16, referred to in the text.

Table 1. Constants and Eddy Characteristics.

Description	Variable	Value	Units
Density, air	ρ_a	1.2	$\mathrm{kg\,m^{-3}}$
Density, seawater	ρ_0	1026	$\mathrm{kg\,m^{-3}}$
Coriolis parameter, 21°N	f	5.21×10^{-5}	$\mathrm{s^{-1}}$
Drag coefficient	c_d	1.18×10^{-3}	
Surface wind speed	U_a	4.7	$\mathrm{m\,s^{-1}}$
Eddy radius of maximum velocity	R	48	km
Maximum azimuthal velocity, cyclone	V	0.222	$\mathrm{m\,s^{-1}}$
Mixed layer depth	H	30	m

Table 2. Summary of Model Runs.

Label	Eddy–Wind Interaction	Tracer Floating Velocity	Eddy Strength Factor	Wind Speed
$\tau(U_w)$	off	1.2×10^{-4} $\mathrm{m\,s^{-1}}$ (10 $\mathrm{m\,d^{-1}}$)	1	4.7 $\mathrm{m\,s^{-1}}$
$\tau(U_w - u_s)$	on	1.2×10^{-4} $\mathrm{m\,s^{-1}}$ (10 $\mathrm{m\,d^{-1}}$)	1	4.7 $\mathrm{m\,s^{-1}}$
w1	on	1.2×10^{-5} $\mathrm{m\,s^{-1}}$ (1 $\mathrm{m\,d^{-1}}$)	1	4.7 $\mathrm{m\,s^{-1}}$
w100	on	1.2×10^{-3} $\mathrm{m\,s^{-1}}$ (100 $\mathrm{m\,d^{-1}}$)	1	4.7 $\mathrm{m\,s^{-1}}$
strong	on	1.2×10^{-4} $\mathrm{m\,s^{-1}}$ (10 $\mathrm{m\,d^{-1}}$)	1.6	4.7 $\mathrm{m\,s^{-1}}$
no wind	-	1.2×10^{-4} $\mathrm{m\,s^{-1}}$ (10 $\mathrm{m\,d^{-1}}$)	1	0

Table 3. Percent Change in Tracer Concentration After 6 Months of Simulation

Label	Tracer Increase
$\tau(U_w - u_s)$	+54%
$\tau(U_w)$	−0.2%
w1	+52%
w100	+76%
strong	+89%

Table 4. Integrated *Trichodesmium* colony abundances. Abundance inside C3 was calculated based on the nearest four 11-km VPR data bins to the eddy center. Abundance inside A3 was calculated based on seven 11-km VPR track bins nearest to the eddy center. n is either the number of 11-km bins included in the calculations based on VPR observations, or the total number of measurements for the calculations based on *Luo et al.* [2012]. Background abundance was estimated as the average along a transect beginning inside C3 and ending at the highest sea level anomaly point sampled in A3. Climatological estimates based on *Luo et al.* [2012] include all available integrated *Trichodesmium* abundances sampled between the months of August and December, 20°N and 29°N, and 70°W and 59°W (see Figure A.3).

Source	Metric	Value
Inside C3, nearest 4 11-km bins		
	mean	12700 colonies m^{-2}
	standard dev.	1400 colonies m^{-2}
	n	4
Inside A3, nearest 7 11-km bins		
	mean	852 colonies m^{-2}
	standard dev.	261 colonies m^{-2}
	n	7
Background estimate, observations (C3 to A3)		
	mean	5010 colonies m^{-2}
	standard dev.	5920 colonies m^{-2}
	n	25
Background estimate, climatology		
	mean	7950 colonies m^{-2}
	standard dev.	6520 colonies m^{-2}
	n	10
	geometric mean	6120 colonies m^{-2}
Percent increase inside C3, relative to:		
	observations (C3 to A3)	153%
	climatology, mean	59.2%
	climatology, geometric mean	107%
	average of C3 and A3 centers	87.4%

Auxiliary Material for

Mesoscale Eddies and *Trichodesmium* spp. Distributions in the Southwestern North Atlantic.

Elise M. Olson

(Woods Hole Oceanographic Institution, Woods Hole, USA)

Dennis J. McGillicuddy

(Woods Hole Oceanographic Institution, Woods Hole, USA)

Glenn R. Flierl

(Department of Earth, Atmospheric and Planetary Sciences, Massachusetts Institute of Technology, Cambridge, Massachusetts, USA)

Cabell S. Davis

(Woods Hole Oceanographic Institution, Woods Hole, USA)

Sonya T. Dyhrman

(Dept. Earth and Environmental Science and the Lamont-Doherty Earth Observatory, Palisades, New York, USA)

John B. Waterbury

(Woods Hole Oceanographic Institution, Woods Hole, USA)

Journal of Geophysical Research – Oceans

Introduction

Three figures are included. The first two relate to the numerical model presented in Section 3.3. The first (Figure A.1) displays the temperature and salinity profiles used to create the initial conditions. The second (Figure A.2) presents the rate of decay of kinetic energy over time for various model runs. The third figure demonstrates regional patterns in integrated *Trichodesmium* colony abundance from the database compiled by *Luo et al.* [2012]. These data were used to

compute one estimate of background colony abundance for the estimation of the observed increase in abundance associated with fall cruise Eddy C3.

1. Auxiliary Material: Potential Temperature and Salinity Profiles

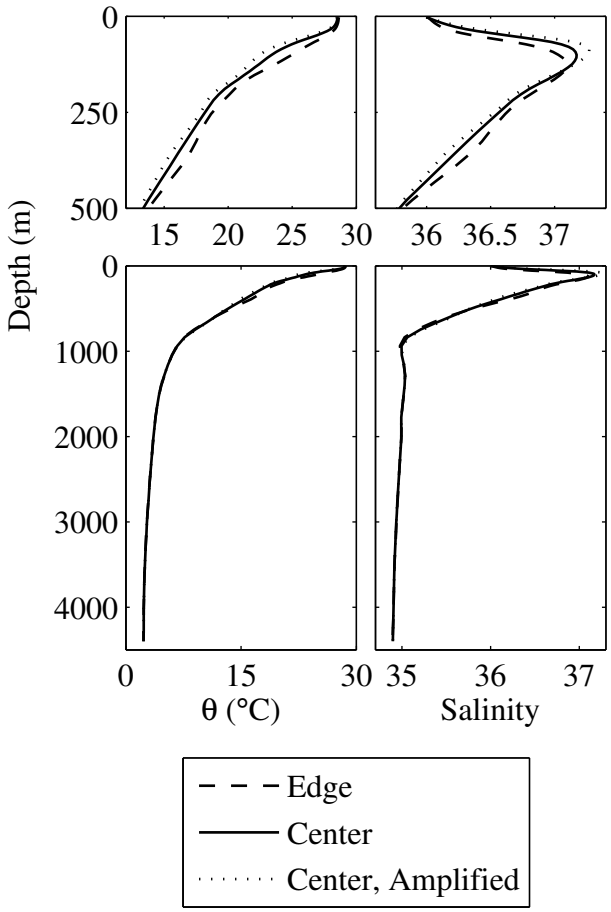

Figure A.1. Potential temperature and salinity profiles used to initialize eddy models, as described in Section 3.3.1.

2. Auxiliary Material: Decay of Kinetic Eddy in Eddy Simulations

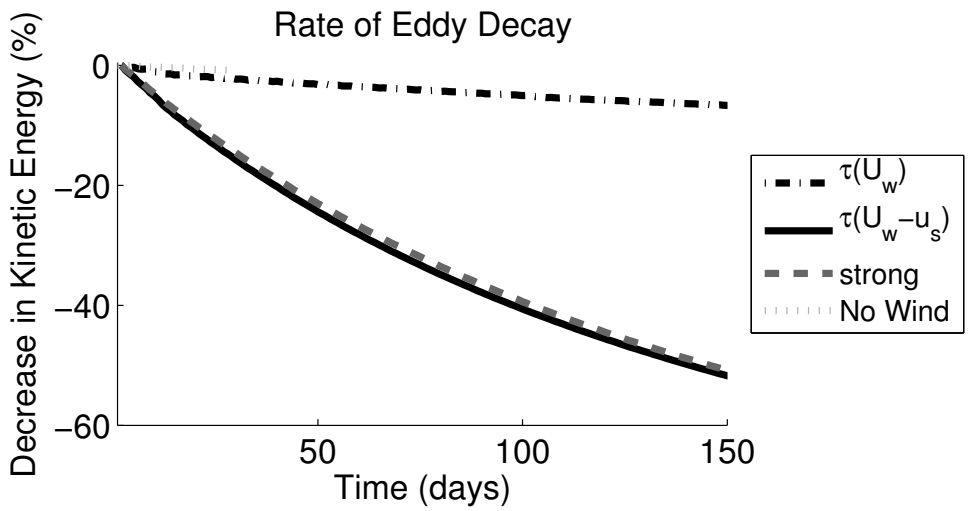

Figure A.2. Relative decay of total kinetic energy over time. Kinetic energy time series were smoothed with a three-day running average to remove the effects of waves, which were not fully resolved by the daily average model output. The fractional rates of decay for the basic and amplified eddies with eddy–wind interaction ("$\tau(U_w - u_s)$" and "strong") were roughly equivalent throughout the six month model runs. Between days 1 and 50, maximum azimuthal geostrophic velocities decreased from roughly 0.23 to 0.17 $\mathrm{m\,s^{-1}}$ in the basic case with eddy–wind interaction ("$\tau(U_w - u_s)$"). Over the same period, in the absence of eddy–wind interaction ("$\tau(U_w)$"), decay was much slower, with maximum eddy velocities remaining roughly constant at 0.241 $\mathrm{m\,s^{-1}}$. A 30-day simulation without wind forcing ("no wind") had the slowest relative rate of decay of kinetic energy over the first month of simulation.

3. Auxiliary Material: Integrated *Trichodesmium* Abundance from *Luo et al.* [2012] Database

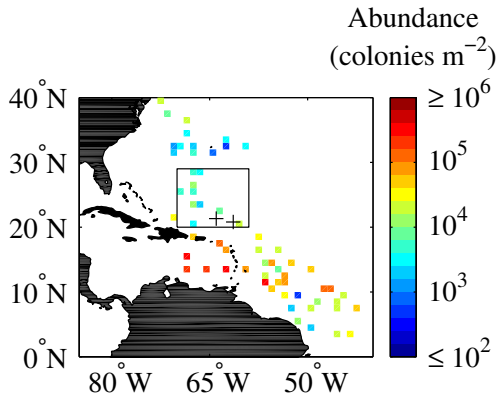

Figure A.3. Gridded integrated *Trichodesmium* colony abundance from the months of August through December from a database compiled by *Luo et al.* [2012]. The boxed region was used to compute mean integrated *Trichodesmium* colony abundance (Table 4) representative of the region and time of year eddies C3 and A3 were sampled. Positions of C3 and A3 at the time of sampling are marked with + signs. The region was chosen to extend farther north based on patterns of *Trichodesmium* abundance and influence of riverine input just to the south of C3 and A3.